



Publication Year	2018
Acceptance in OA@INAF	2020-11-18T14:37:17Z
Title	Swift Observations of Mrk 421 in Selected Epochs. I. The Spectral and Flux Variability in 2005-2008
Authors	Kapanadze, B.; VERCELLONE, STEFANO; ROMANO, Patrizia; Hughes, P.; Aller, M.; et al.
DOI	10.3847/1538-4357/aaa75d
Handle	http://hdl.handle.net/20.500.12386/28418
Journal	THE ASTROPHYSICAL JOURNAL
Number	854



Swift Observations of Mrk 421 in Selected Epochs. I. The Spectral and Flux Variability in 2005–2008

B. Kapanadze^{1,2} , S. Vercellone² , P. Romano² , P. Hughes³ , M. Aller³ , H. Aller³ , O. Kharshiladze⁴,
S. Kapanadze¹, and L. Tabagari¹

¹ E. Kharadze Abastumani Astrophysical Observatory, Ilia State University, Colokashvili Av. 3/5, Tbilisi, 0162, Georgia

² INAF, Osservatorio Astronomico di Brera, Via E. Bianchi 46, I-23807 Merate, Italy

³ Astronomy Department, University of Michigan, Ann Arbor, MI 48109-1107, USA

⁴ Department of Physics, I. Javakishvili State University, Chavchavadze Av. 3, Tbilisi 0128, Georgia

Received 2017 September 23; revised 2017 December 29; accepted 2018 January 2; published 2018 February 13

Abstract

We present detailed results of *Swift* observations of the nearby TeV-detected blazar Mrk 421, based on the rich archival data obtained during 2005 March–2008 June. The best fits of the 0.3–10 keV spectra were mainly obtained using the log-parabolic model, yielding low spectral curvatures expected in the case of the efficient stochastic acceleration of particles. During strong X-ray flares, the position of the synchrotron spectral energy distribution peak E_p was beyond 8 keV for 41 spectra, while it sometimes was situated at the UV frequencies in quiescent states. The photon index at 1 keV exhibited a broad range, and the values $a < 1.70$ were observed during the strong flares, hinting at the possible presence of a jet hadronic component. The spectral parameters were correlated in some periods, expected in the framework of the first- and second-order Fermi accelerations of X-ray emitting particles, as well as in the case of turbulence spectrum. The 0.3–10 keV flux and spectral parameters sometimes showed very fast variability down to the fluctuations by 6–20% in 180–960 s, possibly related to the small-scale turbulent areas containing strongest magnetic fields. X-ray and very high-energy fluxes often showed correlated variability, although several occurrences of more complicated variability patterns are also revealed, indicating that the multifrequency emission of Mrk 421 could not be generated in a single zone.

Key words: BL Lacertae objects: individual (Mrk421)

Supporting material: figure sets, machine-readable tables

1. Introduction

BL Lacertae objects (BLLs) constitute an extreme class of active galactic nuclei (AGNs) exhibiting weak or absent emission lines, strong flux variability in different spectral bands, compact radio structure, superluminal motion of some components, and a very broad continuum ranging from the radio to very high-energy γ -rays ($E > 100$ GeV), that makes them the most frequently detected class of the extragalactic TeV sources.⁵ These properties are most successfully explained as arising from a relativistic jet closely aligned to our line of sight (Urry & Padovani 1995 and references therein).

BLLs show a double-humped spectral energy distribution (SED) in the $\log \nu - \log \nu F_\nu$ plane. Due to the nonthermal and polarized emission in the frequency range of the lower-energy SED component, its origin is widely accepted to be produced by a distribution of relativistic leptons radiating via the synchrotron process (Falomo et al. 2014). Depending on the position of the synchrotron SED peak, E_p , BLLs are divided into two subclasses (Padovani & Giommi 1995 and references therein): high-energy-peaked objects (HBLs, peaking at UV–X-ray frequencies), and low-peaked objects (LBLs, with E_p situated in the infrared-optical part of the spectrum).

However, there is a variety of models for the origin of the SED higher-energy component: (i) an inverse Compton (IC) scattering of synchrotron photons by their “parent” electron–positron population (so-called synchrotron self-Compton model, SSC; Marscher & Gear 1985); (ii) hadronic models incorporating a production of γ -rays by relativistic protons,

either directly (proton synchrotron; Mücke et al. 2003) or indirectly (e.g., synchrotron emission from a secondary electron population; Mannheim 1993). A valid model can be discerned via the intense multiwavelength (MWL) flux variability and inter-band cross-correlation study, which also provides important clues about underlying physical processes, as well as the structure and dynamics of the BLL emission zone. The one-zone SSC model predicts nearly simultaneous variations in both the synchrotron and Compton components, while the multi-zone SSC and hadronic models predict more complicated timing (Fossati et al. 2008).

The nearby HBL source Mrk 421 ($z = 0.03$, Aleksić et al. 2015a) was the first TeV-detected extragalactic object (Punch et al. 1992). Consequently, it was a frequent target of MWL campaigns (see, e.g., Macomb et al. 1995; Fossati et al. 2008; Acciari et al. 2011; Aleksić et al. 2015a; Baloković et al. 2016), which revealed an extreme X-ray and VHE behavior of this source, leading to a great advance in our understanding of the blazar phenomenon. It exhibited the most extreme VHE flares (e.g., a flux increase by a factor of 20–25 in ~ 30 minutes on 1996 May 7; Gaidos et al. 1996), a giant X-ray flare with intra-day X-ray variability by a factor up to nine in 2013 April (Kapanadze et al. 2016a, hereafter Paper I), and variability by more than one order of magnitude on yearly timescales at longer wavelengths (Ahnen et al. 2016).

In this paper, we present the results of a detailed spectral analysis, based on the rich archival data obtained with X-ray Telescope (XRT, Burrows et al. 2005) onboard the satellite *Swift* (Gehrels et al. 2004) during 2005 March–2008 June. Although the majority of these data were included in

⁵ <http://tevcat.uchicago.edu/>

Table 1
Summary of the XRT and UVOT Observations in 2005 March–2008 June

ObsID	Obs. Start—End (UTC)	Exp. (s)	CR (cts s ⁻¹)	UVW1 (mag)	UVW1 (mJy)	UVM2 (mag)	UVM2 (mJy)	UVW2 (mag)	UVW2 (mJy)
(1)	(2)	(3)	(4)	(5)	(6)	(7)	(8)	(9)	(10)
30352001	2006 Jan 02 10:52:00 Jan 03 14:07:11	2192	67.76(0.23)	11.87(0.04)	15.91(0.59)	12.09(0.04)	11.12(0.24)	11.82(0.04)	13.74(0.45)
30252002	2006 Jan 04 10:42:00 Jan 04 14:09:23	4553	88.22(0.17)	11.85(0.03)	16.20(0.52)	12.11(0.03)	10.91(0.17)	11.82(0.03)	13.74(0.29)
30252003	2006 Jan 05 10:48:00 Jan 05 14:10:56	1538	71.95(0.23)	11.86(0.04)	16.05(0.52)	12.13(0.04)	10.71(0.17)	11.83(0.03)	13.62(0.28)
30252004	2006 Jan 07 09:44:01 Jan 08 12:48:15	4741	52.64(0.11)	11.79(0.07)	17.13(0.59)	11.96(0.04)	12.54(0.22)	11.74(0.04)	15.22(0.45)

Note. The columns are as follows: (1) observation ID; (2) observation start and end (in coordinated universal time, UTC); (3) exposure (in seconds); (4) observation-binned count rate (CR) with its error; (5)–(10) de-reddened UVOT magnitudes and fluxes.

(This table is available in its entirety in machine-readable form.)

published papers (see Tramacere et al. 2009; Acciari et al. 2011; Aleksić et al. 2012), the high X-ray brightness of the source and excellent instrumental capabilities of *Swift*-XRT (good photon statistics and low background counts) allow us to perform a detailed study of X-ray spectral and flux variability on timescales shorter than 1 ks. Note that Acciari et al. (2011) and Aleksić et al. (2012) were mostly focused on TeV-band variability, searching for the MWL correlations and SED modeling, and no detailed X-ray spectral and flux variability studies were performed. Although the study of Tramacere et al. (2009) (hereafter T09) is focused on the *Swift*-XRT observations between 2006 April and 2006 July to investigate trends between the spectral parameters and an orbit-resolved spectral analysis was performed, the source was very bright and very densely sampled XRT observations were performed. This allows us to carry out even suborbit-resolved spectral analysis (down to timescales as short as 100 s) and search for very fast flux variability on timescales of a few hundred seconds. Moreover, T09 used only the log-parabolic model for the spectral analysis, while many spectra from the aforementioned period do not show a significant curvature and can be fitted with a simple power law (see Section 3.4). Finally, no detailed study of short-term flux and spectral variability was performed within those studies, while our analysis has revealed extreme behavior on these timescales. Furthermore, we compare the obtained results to those from the epoch of the unprecedented X-ray flare in 2013 April presented in Paper I and from the period 2013 November–2015 June (Kapanadze et al. 2017a, hereafter Paper II). Using the XRT observations, we also performed a study of the 0.3–10 keV flux variability on diverse timescales and checked its correlation with the simultaneous MWL fluxes obtained with different instruments: Ultraviolet-Optical Telescope (UVOT; Roming et al. 2005) and Burst Alert Telescope (BAT; Barthelmy et al. 2005) onboard *Swift*, All-Sky Monitor (ASM) onboard *Rossi X-ray Timing Explorer* (RXTE, Levine et al. 1996), and ground-based Cherenkov-type and optical telescopes.

The paper is organized as follows. Section 2 describes the data processing and analysis procedures. In Section 3, we provide spectral results. Those related to the MWL flux and spectral variability on diverse timescales are presented in Section 4. We discuss our results in Section 5, and provide our conclusions in Section 6.

2. Observations and Data Reduction

2.1. X-Ray Observations

The source was observed 109 times by XRT between 2005 March 20 and 2008 June 12, with a total exposure of 367.4 ks. The information about each pointing and the corresponding count rates are provided in Table 1.^{6,7} The raw event files were reduced, calibrated, and cleaned with the XRTPIPELINE script incorporated in the XRTDAS package (a part of HEASOFT v. 6.21, developed at ASI Science Data Center and distributed by HEASARC) by applying the standard filtering criteria and the latest calibration files of *Swift* calibration database (CALDB) v.20170306.

We selected the events with the 0–2 grades for the Windowed Timing (WT) mode, and the grade of 0–12 was used for the Photon Counting (PC) observations (used only three times). In both regimes, the selection of the source and background extraction regions, correction of count rates for pile-up and other effects (bad/hot pixels, vignetting) was performed with the package XSELECT, following the recipes described in detail in Paper I. The background-subtracted light curves were constructed using different time bins (see Section 4). In the WT mode, the pile-up correction was applied when the 0.3–10 keV count rate was close to or higher than 100 cts s⁻¹ (Romano et al. 2006).

From the daily-binned BAT data, obtained within the *Swift*-BAT Hard X-ray Transient Monitor program⁸ (Krimm et al. 2013) and provided by the BAT team, we used only those corresponding to the detection of the source with 5 σ significance (the threshold generally accepted for coded-mask devices) to study a variability of the 15–150 keV flux. However, we also plotted the data corresponding to their detection with 3 σ significance in Figure 4(c) (used by some authors for flux variability study; see, e.g., Horan et al. 2009).

2.2. UVOT Observations

The source was observed in the ultraviolet bands UVW₁, UVM₂, and UVW₂ at the central wavelengths of 2600 Å, 2200 Å, and 193 Å, respectively (along with the 0.3–10 band)

⁶ The three leading zeros in observation IDs (ObsID) are omitted everywhere in the paper.

⁷ Tables 1, 2, 5, and 7 are available, in their entirety, in machine-readable form.

⁸ <http://swift.gsfc.nasa.gov/results/transients/weak/Mrk421/>

Table 2
Results of the Spectral Analysis with the Log-parabolic Model

ObsID (1)	a (2)	b (3)	E_p (4)	$10 \times K$ (5)	χ_r^2/dof (6)	$\log F_{0.3-2 \text{ keV}}$ (7)	$\log F_{2-10 \text{ keV}}$ (8)	$\log F_{0.3-10 \text{ keV}}$ (9)	HR (10)
35014001 Orbit 2	2.55(0.02)	0.15(0.04)	0.02(0.01)	1.03(0.01)	1.06/218	-9.43(0.01)	-9.97(0.01)	-9.32(0.01)	0.29(0.01)
Orbit 4	2.51(0.02)	0.16(0.06)	0.03(0.01)	1.09(0.02)	1.05/179	-9.42(0.01)	-9.93(0.02)	-9.30(0.01)	0.31(0.01)
Orbit 5	2.49(0.02)	0.12(0.04)	0.02(0.01)	1.16(0.02)	0.89/211	-9.40(0.01)	-9.88(0.02)	-9.27(0.01)	0.33(0.01)
Orbit 6	2.43(0.02)	0.13(0.04)	0.02(0.01)	1.26(0.02)	1.05/224	-9.37(0.01)	-9.81(0.01)	-9.23(0.01)	0.36(0.01)

Note. The E_p values (Column 4) are given in keV; unabsorbed 0.3–2 keV, 2–10 keV, and 0.3–10 keV fluxes (Columns 7–9)—in $\text{erg cm}^{-2} \text{s}^{-1}$.

(This table is available in its entirety in machine-readable form.)

and an average duration of 150 s in each filter, ranging between 50 and 900 s. Unfortunately, Mrk 421 was not targeted with UVOT during 2005 April–November or 2007 March–2008 January, and only a few times in 2006 April–July (see Table 1). The observations were carried out in the image mode, where the image is accumulated onboard, discarding the photon timing information within each exposure to reduce the telemetry volume and the transmission time.

The photometry for the sky-corrected images obtained in these bands was performed using the `UVOTSOURCE` tool (maintained by the `HEASOFT` package) and the calibration files included in the CALDB v.20170130. The measurements were done using a 20 arcsec radius because the source was very bright in these bands. When the source was brighter than 12 mag, a pile-up was estimated and the corresponding correction was performed using the recipe provided in Page et al. (2013). The magnitudes were then corrected for Galactic absorption, converted into milli-Janskys (mJy), and corrected for the host contribution according to the recipe provided in Paper II (see Table 1 for the results).

3. Spectral Analysis

The 0.3–10 keV spectral analysis was performed by means of the XSPEC package (Arnaud 1996), using the latest response matrix from the XRT calibration files from *Swift* CALDB, as well as ancillary response files generated via the XRTMKARF task (to account for the aforementioned effects). The instrumental channels were combined to include at least 20 photons per bin using the `GRPPHA` task to yield a spectrum valid for the χ^2 -statistics. We fixed the hydrogen column density to the Galactic value $N_H = 1.9 \times 10^{20} \text{ cm}^{-2}$ (Kalberla et al. 2005), and performed a fit of the reduced spectra using different models, generally applicable for blazar X-ray spectra (see Section 3.1).

For each spectrum, the model validity was checked by means of reduced chi-squared (χ_r^2), distribution of the residuals, and F-test. We extracted the spectra from separate orbits of the particular ObsID when it was impossible to use the same source and/or background extraction regions for all orbits, or the source showed a flux variability during this observation. We adopted the same method even for a single orbit when the flux varied within it, or when there was no satisfactory value of χ_r^2 for the spectrum extracted from the whole orbit. In similar situations, we extracted the spectra even from the segments of the particular orbit, especially in higher X-ray states. The task `EDITMOD` was used to remove the absorption component in order to measure de-absorbed 0.3–2 keV, 2–10 keV, and 0.3–10 keV fluxes, as well as their errors (in logarithmic units). The hardness ratio (HR) was calculated as

$\text{HR} = F_{2-10 \text{ keV}}/F_{0.3-2 \text{ keV}}$, where the quantities $F_{2-10 \text{ keV}}$ and $F_{0.3-2 \text{ keV}}$ stand for the unabsorbed 2–10 keV and 0.3–2 keV fluxes, respectively. This parameter is useful to study spectral variability and reveal spectral trends during X-ray flares when the spectra extracted from different observations are fitted with different spectral models (see the next subsections).

3.1. Spectral Curvature

For the majority of the 0.3–10 keV spectra in 2005 March–2008 June (870 out of 1200 spectra), a simple power law, $F(E) = KE^{-\Gamma}$ (with Γ , the photon index throughout the observation band; K , the normalization factor), was excluded at the 99.99% confidence level, and the log-parabolic model (Massaro et al. 2004, hereafter M04)

$$F(E) = K(E/E_1)^{-(a+b \log(E/E_1))} \quad (1)$$

was clearly preferred by the aforementioned tests (with E_1 , the pivot energy fixed to 1 keV; a , the photon index at the energy E_1 ; b , the curvature parameter). In addition, this model showed a better fit to the aforementioned spectra than a broken power law.⁹ By means of the best-fit values of the parameters a and b , the position of the SED peak and the flux at the peak are calculated as¹⁰ (M04)

$$E_p = E_1 10^{(2-a)/2b} \text{ keV}, \quad (2)$$

$$S_p = 1.6 \times 10^{-9} K 10^{(2-a)^2/4b} \text{ erg m}^{-2} \text{ s}^{-1}. \quad (3)$$

The results of the spectral analysis performed using the log-parabolic model are provided in Table 2. The distributions of spectral parameters and their properties observed during the whole period 2005–2008, as well as in its separate parts (“Periods” 1–6, selected depending on the occurrence of enhanced X-ray activity of Mrk 421; see the caption of Table 3) are presented in Figure 1 and Table 3, respectively. For comparison, we have also included the results from the 2013 April period here.

The curved 0.3–10 keV spectra mostly showed low values of parameter b : 57% of the values from the range $b = 0.07$ –0.47 were smaller than $b = 0.20$, and only 23 spectra (2.6%) yielded $b > 0.35$ (see Figure 1(a), first panel). In 2005 March–2008 June, the parameter b mostly showed relatively small values: 96% of the log-parabolic spectra yielded $b < 0.35$. Note that the source showed a similar distribution of this parameter in the epoch of the giant X-ray flare in 2013 April and during 2013

⁹ See <https://heasarc.gsfc.nasa.gov/xanadu/xspec/manual/XSmodelBknpower.html>.

¹⁰ The corresponding uncertainties are calculated by propagation of the errors related to the parameters included in each equation.

Table 3
Distribution of Spectral Parameters in Different Periods

Par. (1)	Minimum (2)	Maximum (3)	Mean (4)	Skewness (5)
2005–2008				
b	0.09	0.47	0.21	0.60
a	1.62	2.63	2.07	0.38
E_p	0.80	7.94	2.71	0.85
Γ	1.68	2.74	1.91	0.26
HR	0.22	1.49	0.79	0.04
Periods 1–2				
b	0.07	0.29	0.19	0.17
a	1.90	2.56	2.09	0.50
E_p	0.87	1.83	1.31	0.27
Γ	2.13	2.74	2.58	
HR	0.23	0.93	0.59	0.23
Period 3				
b	0.09	0.22	0.14	0.57
a	1.69	2.15	1.89	–0.35
E_p	0.83	7.94	2.88	0.90
Γ	1.68	2.15	1.89	0.08
HR	0.60	1.49	0.98	0.59
Period 4				
b	0.12	0.47	0.28	0.30
a	2.01	2.56	2.24	0.61
E_p	0.80	...	0.88	0.74
Γ	1.89	2.32	2.25	...
HR	0.25	0.68	0.47	–0.30
Periods 5–6				
b	0.07	0.34	0.20	0.41
a	1.62	2.33	2.01	–0.39
E_p	0.81	7.94	3.18	...
Γ	1.78	1.88	1.84	...
HR	0.22	1.14	0.75	0.63
2013 April				
b	0.09	0.47	0.22	0.31
a	1.68	2.55	2.00	0.53
Γ	1.70	2.35	1.99	0.10
HR	0.41	1.31	0.76	0.37

Note. Period 1: 2005 March 1–September 3; Period 2: 2005 October 2–2006 March 22; Period 3: 2006 April 17–2006 July 27; Period 4: 2007 October 6 to 2008 January 24; Period 5: 2008 January 25–April 17; Period 6: 2008 April 26–June 13. Minimum and maximum values are listed in columns 2 and 3, respectively. Mean value is in column 4, and skewness is the last column. The values corresponding to a detection below 3σ (parameter b) and upper limits to E_p are not included here.

November–2014 May, while the spectral curvature generally was larger in 2015 January–June (see Figure 6 and Papers I–II).

The spectra from Period 3 exhibited the lowest curvatures with a mean value $\bar{b} = 0.14$ and with a positive skewness indicating a shift of the distribution toward values lower than \bar{b} (3rd panel). In contrast, the narrowest synchrotron SEDs (i.e., the largest curvatures) are found in Period 4, which showed a mean value twice as large, but smaller skewness (see the fourth panel of Figure 1(a) and Table 3). Note that all the values larger than $b = 0.35$ belong to this period.

The parameter b showed a weak positive correlation with photon index at 1 keV (see Figure 2(a) and Table 4 for the Spearman coefficient ρ and corresponding p -value), and very weak anti-correlations with the position of the synchrotron SED and with unabsorbed 0.3–10 keV flux (see Figure 2(b) and (c) and Section 5.3 for the discussion). Note that we restricted the search for the correlation $b-E_p$ to the spectra with $E_p \geq 0.8$ keV and $E_p \leq 8$ keV (as explained below). This anti-correlation was found with 99% confidence level only for Periods 5 and 6. The correlations $a-b$ and $b-F_{0.3-10\text{keV}}$ are revealed only for Periods 2 and 3.

3.2. Photon Index

The photon index at 1 keV showed a very wide range of values during 2005–2008: $\Delta a = 1.01$, with the smallest value of $a = 1.62$, and 46% of the spectra were harder than $a = 2$ (Figure 1(b), first panel). Note that this percentage was smaller in 2013 January–May (39%; Paper I) and in 2013 November–2015 June (20%; Paper II). Note also that 87% of the 0.3–10 keV spectra from the period 2006 April–July showed $a < 2$, and this percentage is significantly higher than that shown during the giant X-ray flare in 2013 April (61%).

The majority of these hard spectra (65%) belong to Period 3, with a mean value $\bar{a} = 1.89$ (see the 3rd panel of Figure 1(b)). For other periods, the mean value ranged between $\bar{a} = 1.90$ (Period 6) and $\bar{a} = 2.30$ (Period 1). However, the softest spectra are derived from the nine observations performed between 2006 December 5 and 2007 May 12: $\bar{a} = 2.42$ and the softest value $a = 2.63$ during the whole 2005 March–2008 June Period. Period 6 is characterized by the widest range of the photon index $\Delta a = 0.71$.

Figure 2(d) exhibits an anti-correlation between the parameter a and 0.3–10 keV flux, implying that the source mostly followed a “harder-when-brighter” trend during 2005–2008. However, samples belonging to the particular periods show different slopes, leading to the significant scatter of the data points in the $a-F_{0.3-10\text{keV}}$ plane. Although the sample from the whole Period 6 follows the general “harder-when-brighter” trend, the subsample of the spectra extracted from orbits 3–21 of ObsID 30352099 show an exception to this trend: on average, they are the hardest ($a = 1.62$ – 1.81) and yield the largest 0.3–10 keV fluxes (see Table 2), but their subsample exhibits a weak positive photon index–flux correlation, and is thus an outlier from the whole sample in the $a-F_{0.3-10\text{keV}}$ plane. As for the subsamples from other periods, the “harder-when-brighter” trend was the strongest in Period 2, while the source followed it weakly in Periods 4 and 5 (see Table 4). The softest spectra from the period 2006 December–2007 May also follow the aforementioned trend, and they yield the one of the lowest values of unabsorbed 0.3–10 keV flux during the whole 2005 March–2008 June period.

3.3. The Position of the SED Peak

The position of the SED peak showed a very wide range between $E_p = 0.02$ keV and $E_p = 22.4$ keV. Note that 29 spectra showed the E_p values larger than 10 keV (see Figure 3 for the corresponding SEDs). Of these spectra with high E_p , 90% belong to Period 3 and other three spectra to Period 6. However, the SED peaks of the spectra with $E_p \gtrsim 8$ keV (about 5% of the log-parabolic spectra) are poorly constrained

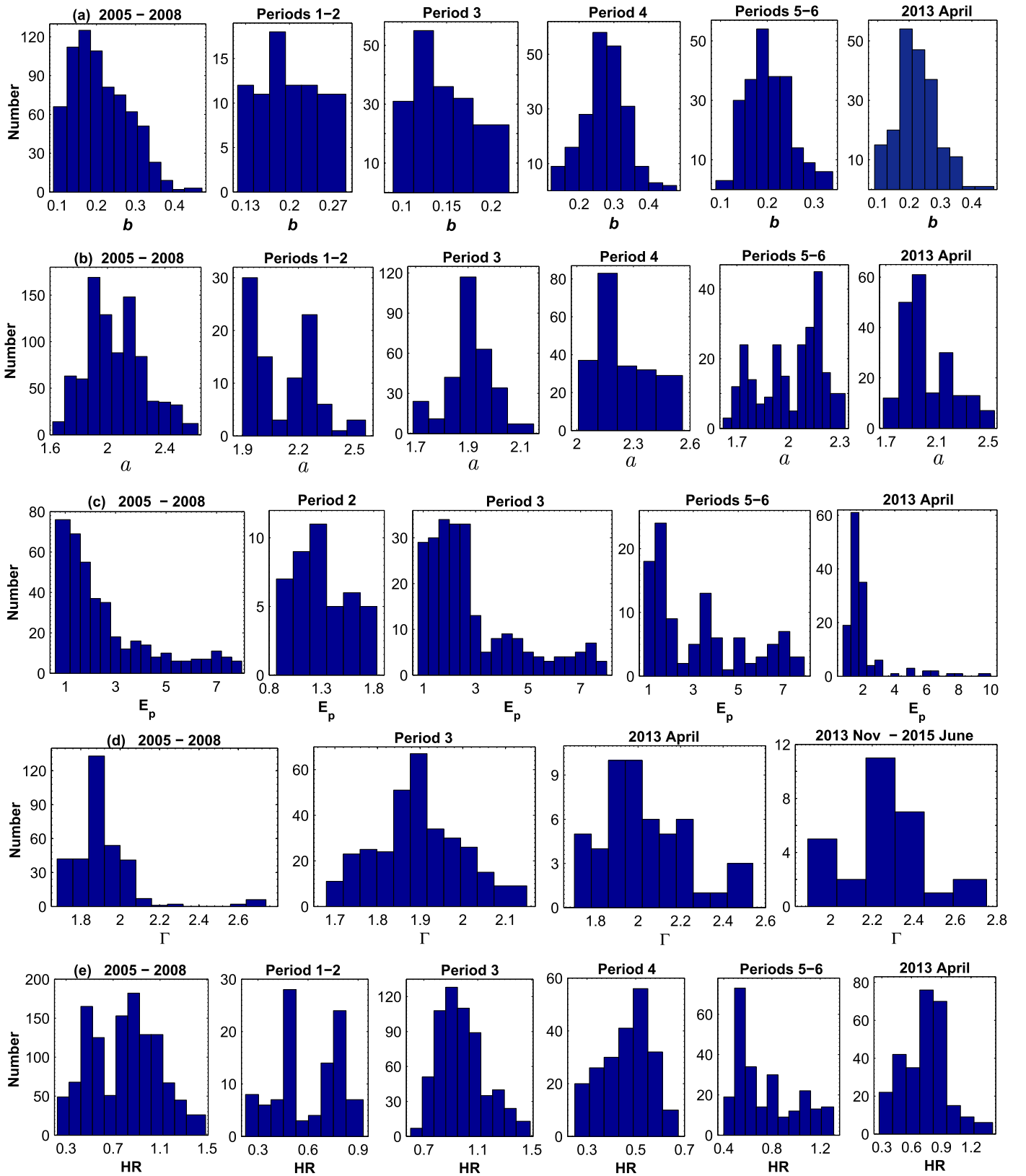


Figure 1. Distribution of the values of spectral parameters in different periods.

by the observational data; because these spectra show the photon indices considerably smaller than $a = 2$, these values should be considered as lower values to the intrinsic position of the synchrotron SED peak. Moreover, the values $E_p \lesssim 0.8$ keV

(48% of log-parabolic spectra), derived from the spectra with photon indices considerably higher than $a = 2$, are systematically higher than those obtained from the contemporaneous broadband SEDs by means of the fit with the log-parabolic

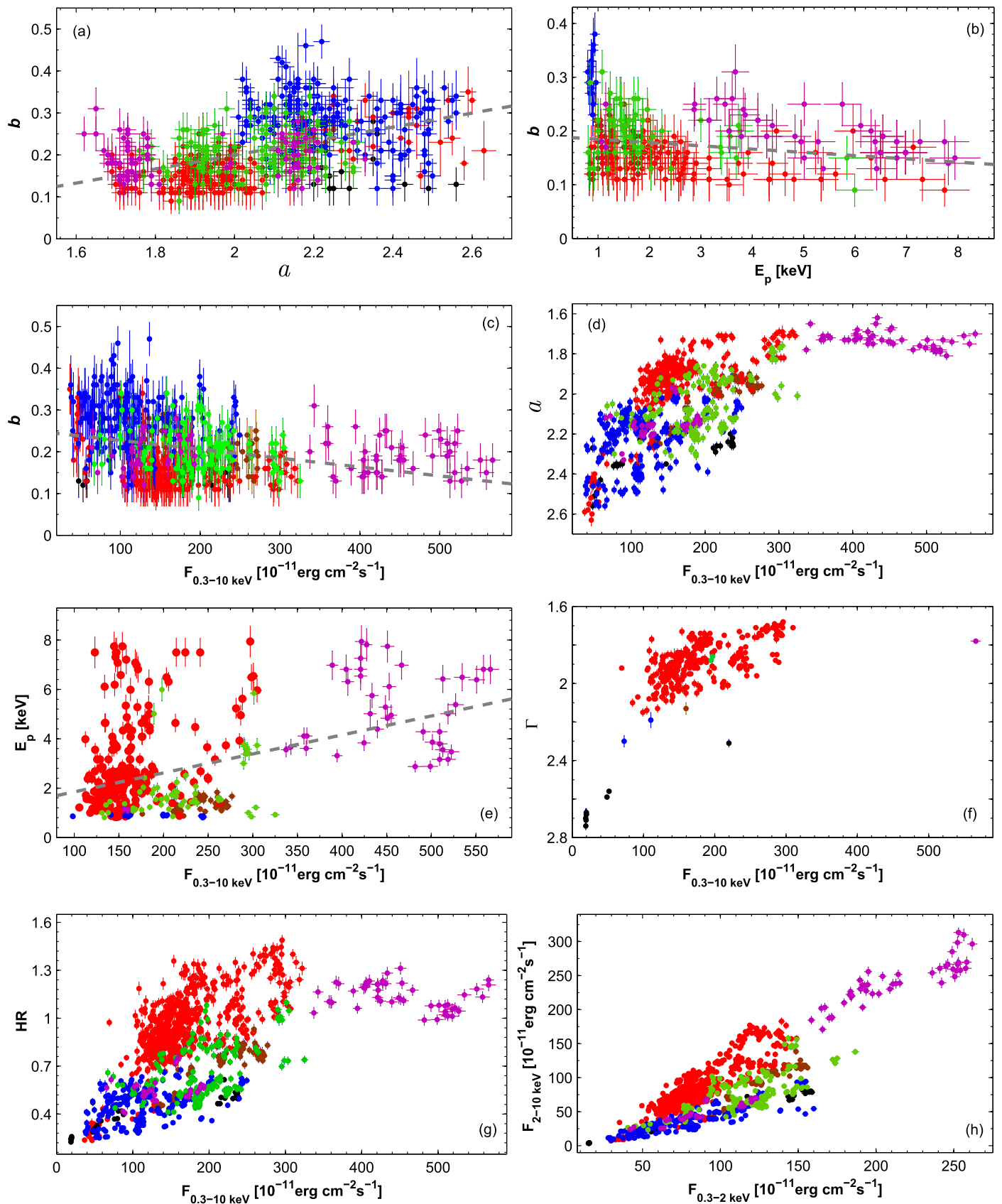


Figure 2. Correlation between the spectral parameters and X-ray fluxes. The colored points correspond to the different periods presented in Table 6 as follows: black—Period 1; brown—Period 2; red—Period 3; blue—Period 4; green—Period 5; purple—Period 6. Gray dashed lines in panels (a), (b), and (e) represent linear fits to scatter plots.

Table 4
Correlations between Spectral Parameters and Multiband Fluxes

Quantities	ρ	p
2005–2008		
b and a	0.41(0.09)	5.17×10^{-7}
b and E_p	-0.21(0.09)	3.22×10^{-3}
b and $F_{0.3-10 \text{ keV}}$	-0.26(0.08)	1.01×10^{-4}
a and $F_{0.3-10 \text{ keV}}$	-0.57(0.06)	5.89×10^{-10}
E_p and $F_{0.3-10 \text{ keV}}$	0.31(0.09)	1.70×10^{-5}
$\log E_p$ and $\log S_p$	0.42(0.10)	6.35×10^{-8}
Γ and $F_{0.3-10 \text{ keV}}$	-0.58(0.06)	2.24×10^{-10}
HR and $F_{0.3-10 \text{ keV}}$	0.53(0.06)	4.47×10^{-9}
$F_{0.3-2 \text{ keV}}$ and $F_{2-10 \text{ keV}}$	0.74(0.04)	5.44×10^{-13}
$F_{0.3-10 \text{ keV}}$ and F_{VHE}	0.60(0.08)	4.67×10^{-10}
F_{BAT} and F_{ASM}	0.53(0.09)	8.00×10^{-8}
F_{ASM} and F_{VHE}	0.45(0.08)	2.13×10^{-9}
F_{UVW1} and F_{UVW2}	0.89(0.02)	$< 10^{-15}$
Period 1		
a and $F_{0.3-10 \text{ keV}}$	-0.53(0.10)	4.01×10^{-5}
Γ and $F_{0.3-10 \text{ keV}}$	-0.67(0.05)	4.88×10^{-11}
HR and $F_{0.3-10 \text{ keV}}$	0.69(0.05)	4.02×10^{-11}
$F_{0.3-2 \text{ keV}}$ and $F_{2-10 \text{ keV}}$	0.83(0.04)	$< 10^{-15}$
Period 2		
b and a	0.25(0.09)	4.99×10^{-4}
b and $F_{0.3-10 \text{ keV}}$	-0.30(0.10)	8.19×10^{-5}
a and $F_{0.3-10 \text{ keV}}$	-0.79(0.04)	3.03×10^{-14}
E_p and $F_{0.3-10 \text{ keV}}$	0.34(0.12)	8.44×10^{-5}
$\log E_p$ and $\log S_p$	0.42(0.10)	6.35×10^{-8}
HR and $F_{0.3-10 \text{ keV}}$	0.77(0.04)	8.41×10^{-14}
$F_{0.3-2 \text{ keV}}$ and $F_{2-10 \text{ keV}}$	0.91(0.02)	$< 10^{-15}$
Period 3		
b and a	0.29(0.09)	3.15×10^{-5}
a and $F_{0.3-10 \text{ keV}}$	-0.65(0.05)	4.19×10^{-12}
b and $F_{0.3-10 \text{ keV}}$	-0.35(0.10)	2.30×10^{-5}
E_p and $F_{0.3-10 \text{ keV}}$	0.29(0.12)	3.70×10^{-4}
$\log E_p$ and $\log S_p$	0.53(0.09)	9.34×10^{-10}
Γ and $F_{0.3-10 \text{ keV}}$	-0.56(0.05)	6.67×10^{-10}
HR and $F_{0.3-10 \text{ keV}}$	0.55(0.05)	9.54×10^{-10}
$F_{0.3-2 \text{ keV}}$ and $F_{2-10 \text{ keV}}$	0.79(0.04)	2.24×10^{-14}
Period 4		
a and $F_{0.3-10 \text{ keV}}$	-0.35(0.09)	6.77×10^{-6}
HR and $F_{0.3-10 \text{ keV}}$	0.38(0.08)	1.48×10^{-6}
$F_{0.3-2 \text{ keV}}$ and $F_{2-10 \text{ keV}}$	0.85(0.03)	$< 10^{-15}$
Period 5		
b and E_p	-0.23(0.10)	1.05×10^{-3}
a and $F_{0.3-10 \text{ keV}}$	-0.40(0.08)	5.56×10^{-7}
$\log E_p$ and $\log S_p$	0.33(0.12)	1.01×10^{-5}
HR and $F_{0.3-10 \text{ keV}}$	0.41(0.06)	2.20×10^{-7}
$F_{0.3-2 \text{ keV}}$ and $F_{2-10 \text{ keV}}$	0.65(0.05)	7.67×10^{-12}
Period 6		
b and E_p	-0.48(0.07)	1.49×10^{-87}
a and $F_{0.3-10 \text{ keV}}$	-0.61(0.06)	6.43×10^{-11}
$\log E_p$ and $\log S_p$	0.73(0.09)	2.75×10^{-14}
HR and $F_{0.3-10 \text{ keV}}$	0.58(0.06)	4.00×10^{-10}
$F_{0.3-2 \text{ keV}}$ and $F_{2-10 \text{ keV}}$	0.89(0.03)	$< 10^{-15}$

Table 4
(Continued)

Quantities	ρ	p
2013 April		
b and E_p	-0.26(0.11)	1.70×10^{-3}
a and $F_{0.3-10 \text{ keV}}$	-0.63(0.05)	5.67×10^{-12}
Γ and $F_{0.3-10 \text{ keV}}$	-0.80(0.04)	2.89×10^{-12}
HR and $F_{0.3-10 \text{ keV}}$	0.65(0.06)	4.35×10^{-11}
$F_{0.3-2 \text{ keV}}$ and $F_{2-10 \text{ keV}}$	0.88(0.03)	$< 10^{-15}$
$F_{0.3-10 \text{ keV}}$ and F_{FACT}	0.78(0.12)	0.014

Note. Fluxes denoted by “ F_i ” for the particular i -band) in different periods.

function (introduced by Landau et al. 1986)

$$\log \nu F_\nu = A(\log \nu)^2 + B(\log \nu) + C. \quad (4)$$

Therefore, these values also should be considered as upper limits, and consequently they (as well as those higher than 8 keV) were not used when searching for correlations of E_p with other spectral parameters or with the 0.3–10 keV flux. All log-parabolic spectra from Period 1, 2006 December–2007 May and 93% of those from Period 4 are characterized by $E_p < 0.8$ keV. In contrast, 91% of the log-parabolic spectra from Period 3 show their synchrotron SED peaks at energies higher than 0.8 keV.

Fifty-nine percent of the values with $0.8 \text{ keV} \leq E_p \leq 8 \text{ keV}$ (i.e., the spectra with well-constrained synchrotron SEDs) are included in Period 3, and the mean value $\bar{E}_p = 2.88 \text{ keV}$ (see Figure 1(c)). This period also comprises the majority of the hard X-ray peaking spectra (i.e., $E_p > 2 \text{ keV}$; 148 out of 205). In contrast, Periods 2 and 4 show $E_p < 1.83 \text{ keV}$ and $E_p < 0.96 \text{ keV}$. This parameter shows a weak positive correlation with the 0.3–10 keV flux, which was observed separately in Periods 2 and 3 (see Figure 2(e) and Table 4). Moreover, the spectra that peak beyond 8 keV yield 0.3–10 keV fluxes, which are significantly higher than $9.8 \times 10^{-10} \text{ erg cm}^{-2} \text{ s}^{-1}$ (the weighted mean value in 2005–2008).

3.4. Power-law Spectra and Hardness Ratio

Table 5 presents the results for 330 spectra in 2005–2008, which do not exhibit a significant curvature: the parameter b is close to zero and/or detected with $\sim 1\sigma$ significance, and the fit with the log-parabolic model did not give better statistics than that with the simple power-law. Therefore, the latter model was chosen for these spectra. The 0.3–10 keV photon index, derived from these spectra, also showed a wide range of values $\Delta\Gamma = 1.06$ (see Figure 1(d)) and the hardest value $\Gamma = 1.68$ (derived from the fourth 190 s segment of the fifth orbit of ObsID 30352014). Note that the vast majority of these spectra (96%) and the hardest values of the parameter Γ belong to Period 3.

In many cases, some orbits of the same observation yielded power-law spectra, while those from other orbits showed a curvature and fitted well with the log-parabolic model. This mainly happened with the densely sampled XRT observations during 2006 April 22–24 (ObsID 206476000) and June 14–27 (ObsID 3035208–3035201616). Some orbits yielded both

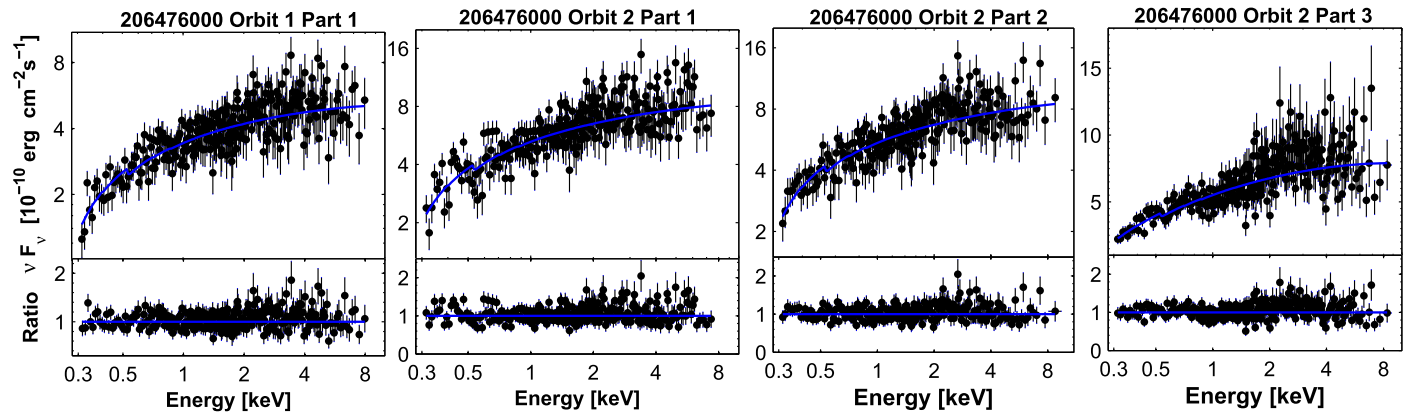


Figure 3. Log-parabolic spectra yielding $E_p > 10$ keV, along with the distribution of the residuals. In each spectrum, a solid line represents the log-normal model defined by Equation (2).

(The complete figure set (seven images) is available.)

log-parabolic and power-law spectra. For example, while the spectra extracted from the second, third, and fourth segments of the first orbit of ObsID 30352011 (each of 200 s) are well-fit with a simple power-law model, those from the first and fifth segments are curved. In total, we extracted 111 spectra from 34 orbits of the most densely sampled observation, and 52% fit well with the power-law model. Furthermore, 91% of the spectra extracted from another densely sampled observation with ObsID 30352014 (June 23) do not show a curvature. Only power-law spectra were extracted from the observations with ObsID 52100007 (Period 1), 52101001 (Period 2), 215769000, and 30352016 (Period 3).

The power-law spectra are found in different brightness states, and they followed a “harder-when-brighter” trend similar to the log-parabolic spectra (see Figure 2(f) and Table 4), although one data point from Period 6 shows a large offset from the general trend.

The values of the hardness ratio, derived from log-parabolic and power-law spectra, showed a wide range of $\Delta HR = 0.92$. Eighty-two percent of the values are larger than $HR = 0.5$, and 315 spectra (27%) show $HR \geq 1$ (Figure 1(e) and Table 3; all spectra presented in Figure 3 yield HR values above this threshold). Note that the spectra with a hardness ratio larger than $HR = 1$ were much more rarely observed in 2013 April and 2013 November–2015 June (8% of all spectra in each period; see Figure 6(Ac), (Bc)).

The mean value of this parameter within the period ranges from $\overline{HR} = 0.34$ (2006 December–2007 May) to $\overline{HR} = 0.98$ (Period 3). The HR –Flux plane brings together power-law and log-parabolic spectra to check the presence of a “harder-when-brighter” spectral trend during the particular flare in some period, or prove whether the power-law and log-parabolic spectra follow this trend differently. A positive correlation between HR and the unabsorbed 0.3–10 keV flux in all periods (Figure 2(g)) confirms the dominance of a “harder-when-brighter” spectral evolution during X-ray flares. This trend was the strongest in Period 2 (see Table 4), and the data points, which correspond to Orbits 3–21 of ObsID 30352099, do not follow the general trend; they form an outlier in the HR –flux plane (similar to parameter a).

4. Flux and Spectral Variability

4.1. Long-term Flux Variability

During 2005 March–2008 June, the 0.3–10 keV flux was highly variable, by a factor of 20, and showed several flares (Figure 4(a)), which are discussed in detail in the next subsection. During the 3.3 year period, the highest and weighted daily-binned count rates were 155.6 cts s^{-1} and 35.5 cts s^{-1} , respectively. The former value was recorded during ObsID 30352099 (2008 June 12–13) and higher rates were observed only on 2013 April 12. Unfortunately, that period was not densely covered by the XRT observations, in contrast to 2013 April. Figure 4(a) shows that the source often exhibited its high X-ray states in the period presented here, similar to the strong X-ray activity epochs observed in 2010, 2013, and 2015. Generally, Mrk 421 was the brightest, as well as one of the most violently variable blazars in X-rays during 2005–2008.

Figure 4(b) present a historical VHE light curve of Mrk 421 (in Crab units), constructed using the data from the observations performed with VERITAS (from the VERITAS website,¹¹ Aleksić et al. 2015a, 2015b; Baloković et al. 2016), MAGIC (Steinke 2012; Preziuso 2013; Aleksić et al. 2015a, 2015b; Ahnen et al. 2016), Whipple¹² (Acciari et al. 2014), and HAGAR (Sinha et al. 2016). The VHE fluxes, provided in units of $\text{ph cm}^{-2} \text{ s}^{-1}$, were converted into Crab units using the relations $1 \text{ Crab} = 1.96 \times 10^{-10} \text{ ph cm}^{-2} \text{ s}^{-1}$ for the data with $E > 200 \text{ GeV}$ (Albert et al. 2008), and $1 \text{ Crab} = 8.08 \times 10^{-11} \text{ ph cm}^{-2} \text{ s}^{-1}$ for those with $E > 400 \text{ GeV}$ (Ahnen et al. 2016). During 2005–2008, the source showed an overall variability by a factor of 26; it underwent a very strong VHE flare during Modified Julian Date MJD 54587–54590 (2008 May) when the source did not exhibit a comparable X-ray activity. Note that the source was often detected with 3σ significance and showed flaring activity in different periods discussed in Section 4.2.

Among 116 detections with 5σ significance of Mrk 421 with BAT during 2004–2015, the majority belong to the period 2005 March–2008 June. The source showed a strong 15–150 keV variability, underwent a strong flare by a factor of ~ 7 , and reached its highest historical brightness during

¹¹ <http://veritas.sao.arizona.edu/veritas-science/veritas-blazar-spectra>

¹² <http://veritas.sao.arizona.edu/veritas-science/mrk-421-long-term-lightcurve>

Table 5
Results of the Spectral Analysis with the Power-law Model

ObsId (1)	Γ (2)	K (3)	χ_r^2/dof (4)	$\log F_{0.3-2\text{ keV}}$ (5)	$\log F_{2-10\text{ keV}}$ (6)	$\log F_{0.3-10\text{ keV}}$ (7)	HR (8)
52100007 Orbit 1	2.68(0.02)	0.41(0.01)	0.93/193	-9.80(0.01)	-10.40(0.01)	-9.71(0.01)	0.25(0.01)
Orbit 2	2.67(0.02)	0.41(0.05)	0.97/180	-9.80(0.01)	-10.39(0.01)	-9.70(0.01)	0.26(0.01)
Orbit 3	2.70(0.05)	0.39(0.01)	1.15/58	-9.82(0.01)	-10.43(0.03)	-9.72(0.01)	0.24(0.02)
Orbit 4	2.74(0.02)	0.39(0.04)	1.00/184	-9.81(0.01)	-10.46(0.01)	-9.72(0.01)	0.23(0.01)

Note. Unabsorbed 0.3–2 keV, 2–10 keV, and 0.3–10 keV fluxes (Columns 5–7) are given in units of $\text{erg cm}^{-2} \text{s}^{-1}$.

(This table is available in its entirety in machine-readable form.)

MJD 53929–53939 (2006 July–August), following the epoch of a high 0.3–10 keV state and hardest spectra (Figure 4(c)).

The source was detected 647 times with 3σ significance, in the 1.5–12 keV band, by *RXTE*-ASM during the period presented here.¹³ It showed a strong variability, with maximum-to-minimum flux ratio $R \approx 15$ (Figure 4(d)). The corresponding light curve exhibits flaring activity on various timescales, and the strongest flares are observed, along with those recorded by XRT, BAT, and Cherenkov-type telescopes.

The source was observed few times with UVOT during 2005–2008. The corresponding light curves present a weaker and slower variability, with a maximum-to-minimum flux ratio of 3.3–4.5 in the *UVW1*–*UVW2* bands, than in the X-ray–TeV energy range (Figure 4(e)). Densely sampled light curves, constructed via *V*- and *R*-band fluxes obtained with the 2.3 m Bock and 1.5 m Kuiper telescopes of Steward observatory,¹⁴ as well as using the archival *V*-band data extracted from the website of American Association of Variable Star Observers (AAVSO),¹⁵ show that the source did not undergo strong optical flares (maximum-to-minimum flux ratio of 3.8–4.7) and exhibited significantly lower brightness states than during 2012–2014 (Figure 4(f)), in contrast to the higher-energy bands.

4.2. Shorter-term Flares

Below, we concentrate on the results from different periods defined in Table 6. The same table gives the summary of each period: maximum 0.3–10 keV count rates, unabsorbed 0.3–10 keV and 2–10 keV, UVOT-band and other MWL fluxes, maximum-to-minimum flux ratios, and fractional variability amplitudes¹⁶ calculated as (Vaughan et al. 2003)

$$F_{\text{var}} = 100((S^2 - \overline{\sigma_{\text{err}}^2})/\overline{F})^{1/2} \%, \quad (5)$$

where S^2 is the sample variance, $\overline{\sigma_{\text{err}}^2}$ —the mean square error, and \overline{F} —the mean flux. The MWL light curves from each subperiod are presented in Figure 5.

In Period 1, the source showed strong variability by a factor of ~ 10 in the 0.3–10 keV band (see Table 6 and Figure 5(a)), accompanied by enhanced VHE activity along with increasing

X-ray brightness. The ASM light curve shows a long-term flare, by a factor of four, after the end of the XRT campaign. In the declining phase of the ASM-band flare, a strong 15–150 keV flare, by a factor of six, was observed with BAT.

In the middle of Period 2, a fast X-ray event with a brightening and subsequent decline by about 50% within 5.9 days was observed (Figure 5(b)). Its peak was accompanied by those in the ASM, BAT, and VHE bands. The MAGIC and Whipple observations revealed other peaks on MJD 53706, 53712, 53731, 53763, 53790, coinciding with those in the ASM and BAT bands.

We observe three X-ray flares by a factor of 2.4–4.5 simultaneously in the XRT and ASM bands around MJD 53847, 53909, and 53931 in Period 3 (Figure 5(c)). The latter was accompanied by a strong BAT-band flare, at a factor of ~ 10 . ASM revealed two other 1.5–12 keV flares, by a factor of 3–5, around MJD 53877 and 53923, which were not covered by XRT observations. The VERITAS and Whipple observations showed three VHE peaks in the epochs of high X-ray states, although no VHE detections were reported during the strongest simultaneous XRT-, ASM-, and BAT-band flare. In Periods 1–3, the *R*-band flux did not show a variability correlated with those observed in the higher-energy bands.

A correlated MWL flaring activity, by a factor of 1.7–2.9, was observed at the end of Period 4 (MJD ~ 54480 ; Figure 5(d)). Before this event, simultaneous high VHE/X-ray states were recorded at MJD ~ 54466 . However, no VHE/UV/optical data are available for the initial part of this period (MJD 54380–54397), when an X-ray flare, by a factor of ~ 3 , was recorded by XRT and ASM. An X-ray flare, recorded during MJD 54500–54510 (Period 5) with XRT and ASM, was also accompanied by enhanced VHE and UV activity, and the *R*-band light curve showed a peak several days earlier (Figure 5(e)). Moreover, we observe strong simultaneous flaring activity in the XRT, ASM, BAT, and VHE bands during MJD 54542–54565 (accompanied by an uncorrelated optical-UV variability).

We observe an uncorrelated VHE/X-ray variability in Period 6: a very strong VHE flare on MJD 54589 (when the source attained its highest VHE state during 2005–2008) was accompanied by lower ASM- and XRT-band states (Figure 5(f)). The next VHE peaks, revealed with the MAGIC observations, coincided with those in the ASM band. However, during the highest XRT-, ASM-, and BAT-band states on MJD 54629–54630, the source was observed only with Whipple detecting it below the 3σ significance. The densely sampled *R*-band light curve does not show a correlated variability with higher-energy bands and exhibits a slow long-term flare, by a factor of 2.3, during the most of this period.

¹³ The data retrieved from <http://xte.mit.edu/asmlc/ASM.html>.

¹⁴ See <http://james.as.arizona.edu/psmith/Fermi/> and Smith et al. (2009) for details. We have de-reddened and converted the corresponding magnitudes into linear fluxes according to Bessel (1979). In the *R*-band, the host contribution is subtracted from the total flux according to Nilsson et al. (2007). The host contribution in the *V*-band was derived according to Fukugita et al. (1995) and subtracted from the total *V*-band flux.

¹⁵ <https://www.aavso.org/data-download>

¹⁶ F_{var} values are not provided in the *UVW1* band because no flux variability was detected due to larger errors and sparsely sampled observations in the majority of the periods.

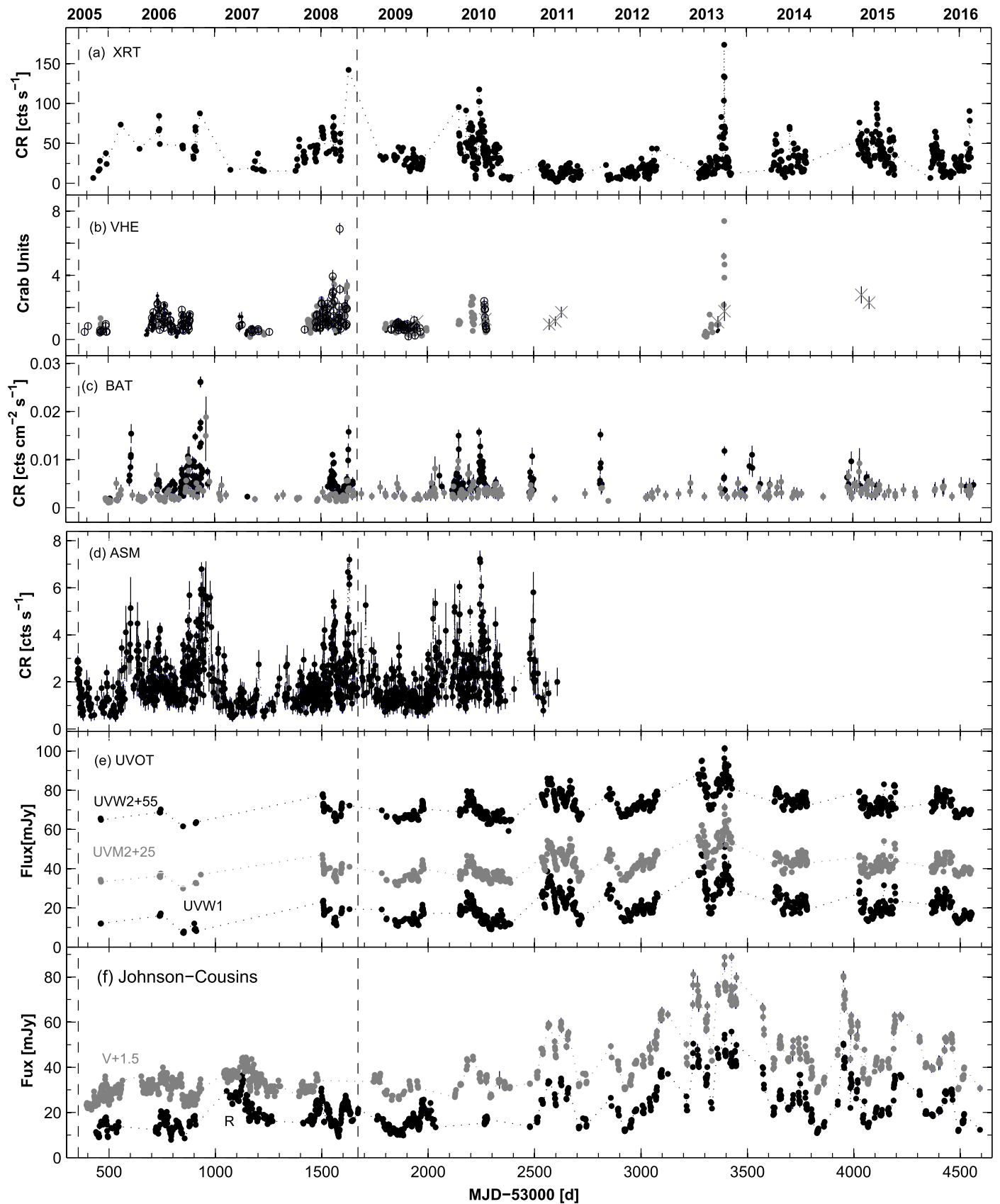


Figure 4. Historical light curves from the daily-binned MWL observations in 2005–2016, performed with XRT (top panel), VHE (panel (b); black points correspond to the VERITAS data, and gray points, circles, and asterisks to those from the MAGIC, Whipple, and HAGAR observations, respectively), BAT (panel (c); black and gray points stand for the detections with 5σ and 3σ significances, respectively), ASM (panel (d)), UVOT (panel (e)), and ground-based optical (panel (f)) telescopes. The period 2005 March–2008 June is indicated by the vertical dashed lines.

Table 6
Summary of the Flux Variability in the XRT, BAT, and UVOT Bands

Per. (1)	MJD (2)	BAT		XRT							UVOT						
		R (3)	F_{var} (4)	$CR_{0.3-10}^{\text{max}}$ (5)	R (6)	F_{var} (7)	F_{2-10}^{max} (8)	R_{2-10} (9)	F_{var} (10)	$F_{0.3-2}^{\text{max}}$ (11)	$R_{0.3-2}$ (12)	F_{var} (13)	R_{W2} (14)	F_{var} (15)	R_{M2} (16)	F_{var} (17)	R_{W1} (18)
1	53430–53559	7.98	48	74.34	9.7	69.6	8.22	23.5	75.3	15.86	10.5	64.3	1.1	4.7	1.1	7.7	1.1
2	53647–53742	2.64	22	88.22	2.0	26.0	13.84	3.5	31.6	15.60	1.8	16.2	1.1	4.7	1.2	7.1	1.1
3	53847–53931	10.67	77	89.67	5.6	42.1	18.30	5.4	35.0	14.89	4.2	23.2	1.3	13.7	2.5	36.8	1.7
4	54380–54484	52.20	3.4	26.5	9.44	11.2	48.4	16.00	5.7	37.8
5	54502–54569	4.00	52	84.70	3.0	25.9	15.78	6.7	35.6	18.66	4.6	22.1	2.5	23.5	2.6	22.0	2.1
6	54588–54630	3.40	37	155.63	5.4	72.6	31.33	12.2	59.9	26.18	6.2	41.7	1.6	14.7	1.4	10.4	1.2

Note. Taken from *Swift* observations of Mrk 421 in different periods defined in columns 1–2. Columns 3–5: maximum 0.3–10 keV flux (in cts s⁻¹), maximum-to-minimum flux ratio, and fractional amplitude (in per cents), respectively; maximum unabsorbed flux (in 10⁻¹⁰ erg cm⁻² s⁻¹), maximum-to-minimum flux ratio and fractional amplitude in the 2–10 keV (Columns 6–8) and 0.3–2 keV (Columns 9–11) Bands; maximum-to-minimum flux ratio and fractional amplitude in the UVW2 (Columns 12–13), UVM2 (Columns 14–15) and UVW1 (Columns 16–17) bands. The errors of F_{var} for the 0.3–10 keV count rate, 0.3–2 keV, and 2–10 keV fluxes are 0.1–0.2, while those in the UVOT and BAT bands are 0.7–1.5 and 2–4, respectively.

4.3. Spectral Variability

Figure 6(Ab) shows that the photon index at 1 keV varied on diverse timescales during 2005 March–2008 June. The largest hardenings were observed during MJD 54382–54387 and MJD 54595–54630 ($\Delta a = 0.52$ –0.71), and the largest softening with $\Delta a = 0.83$ was shown during MJD 53932–54075. This parameter often was variable by $\Delta a = 0.06$ –0.25 on intra-day timescales, generally associated with the intra-day variability (IDV) events and sometimes occurring within 1 ks time intervals (see Section 4.4 and Table 7 for details).

Similar to parameter a , the 0.3–10 keV photon index varied on diverse timescales, and it showed the largest hardening with $\Delta\Gamma = 0.41$ during MJD 53908.02–53909.70, followed by a softening by $\Delta\Gamma = 0.36$ during the next 1.2 day (Figure 6(Ab)). On intra-day timescales, this parameter varied by $\Delta\Gamma = 0.05$ –0.25, associated with the 0.3–10 keV IDVs. The hardness ratio also often varied by 10–77% on intra-day timescales during the 0.3–10 keV IDVs (see Table 7). On longer timescales, this parameter showed the largest increase, by a factor of 3.2, during MJD 54595–630 (Figure 6(Ac)).

The largest variability of the curvature parameter (an increase by $\Delta b = 0.35$) was recorded during MJD 54474–54482. In contrast to the aforementioned parameters, b varied with 3σ significance only once on intra-day timescales (see Figure 6(Ad)) and Section 4.4.2.

The parameter E_p showed an extreme variability during 2005 March–2008 June. Namely, it showed a shift by $E_p > 6$ keV during MJD 53847.36–848.18 (Figure 6(Ae)). Furthermore, the synchrotron SED peak position shifted by $E_p > 6$ keV from 1.9 keV toward higher energies and then moved back to 2.6 keV during MJD 53908.97–53910.07. On intra-day timescales (in addition to the aforementioned extreme event), E_p varied by the amplitudes from 0.6 keV to more than 7.2 keV during the 0.3–10 keV IDVs (see Table 7), mostly moving to higher energies with the increasing flux and vice versa.

4.4. Intra-day Flux and Spectral Variability

During 2005 March–2008 June, the source showed 118 instances of the IDV in the 0.3–10 keV band (defined as a flux change with 99.9% confidence within a day), revealed by means of the χ^2 -statistics. For each event, the values of reduced χ^2 , fractional variability amplitude, and the ranges of the spectral parameters a , b , E_p , and HR are provided in Table 7.

4.4.1. The Fastest IDVs

The source underwent the fastest variability during the 2008 June 12–13 observation (ObsID 30352099), when it declined by 4–10% in 180–1200 s and brightened by 7–8% in 180–600 s (Figure 7(a)). The most dramatic variability occurred during the sixth orbit, when the brightness dropped by 9% in 180 s and then increased by 8% in the same time afterwards. During these instances, the spectrum softened by $\Delta a = 0.08$ –0.10 in 400–500 s and hardened by $\Delta a = 0.07$ in 330 s. In the case of the well-constrained SEDs, the largest variability was $\Delta E_p = 3.2$ keV in 400 s during the third orbit.

As for other very fast IDVs, the brightness increased by 4–19% in 180–900 s (Figure 7(b), (d), (e), (h), (j), (k)) and declined by 6–20% in 180–960 s (Figure 7(c), (f), (g), (i)–(o)). The most extreme variability was observed during the first orbit of ObsID 30352053 (Figure 7(e)): the source brightened twice by 11% and 19% in 240 s and 180 s, respectively. During these events, only E_p parameter showed variability: it moved to lower energies by 0.82–1.30 keV in 500–1100 s and increased by ~ 1.2 keV in 550–600 s (Figures 7(f), (j)).

4.4.2. IDVs from the Extended XRT Observations

Figure 8 presents the light curves of the most densely sampled XRT observations of Mrk 421 in 2006 June 15–25, which lasted 830 ks. Compared to the aforementioned IDVs, the source varied slowly: it brightened by 12–85% in 5.2–47.8 ks and declined by 8–44% in 6–53 ks. The spectra hardened by $\Delta a = 0.08$ –0.26 in 17–47 ks and softened by $\Delta a = 0.09$ –0.21 in 7–40 ks (with a similar variability of the parameter Γ). The source did not follow a “harder-when-brighter” trend within some intervals of this campaign (e.g., during 6.4–12.5 ks since MJD 53901.94). The position of the synchrotron SED peak shifted by $\Delta E_p > 7.2$ keV toward higher energies, moved back to the energies less than 0.8 KeV in 7–41 ks, and often followed the 0.3–10 keV flux variations.

The 0.3–10 keV light curve showed an interesting behavior during the densely sampled observation with 30 orbits and total duration of 167 ks during 2007 October 14–15 (Figure 9(a)): an almost symmetrical profile with a brightness increase–drop by $\sim 50\%$ in about 50 ks and a two-peak maximum. Similar to the aforementioned campaign, the source did not follow a “harder-when-brighter” trend during some intervals. The spectral curvature varied with $\Delta b = 0.22$ and showed higher values around the second peak while the photon index showed a larger

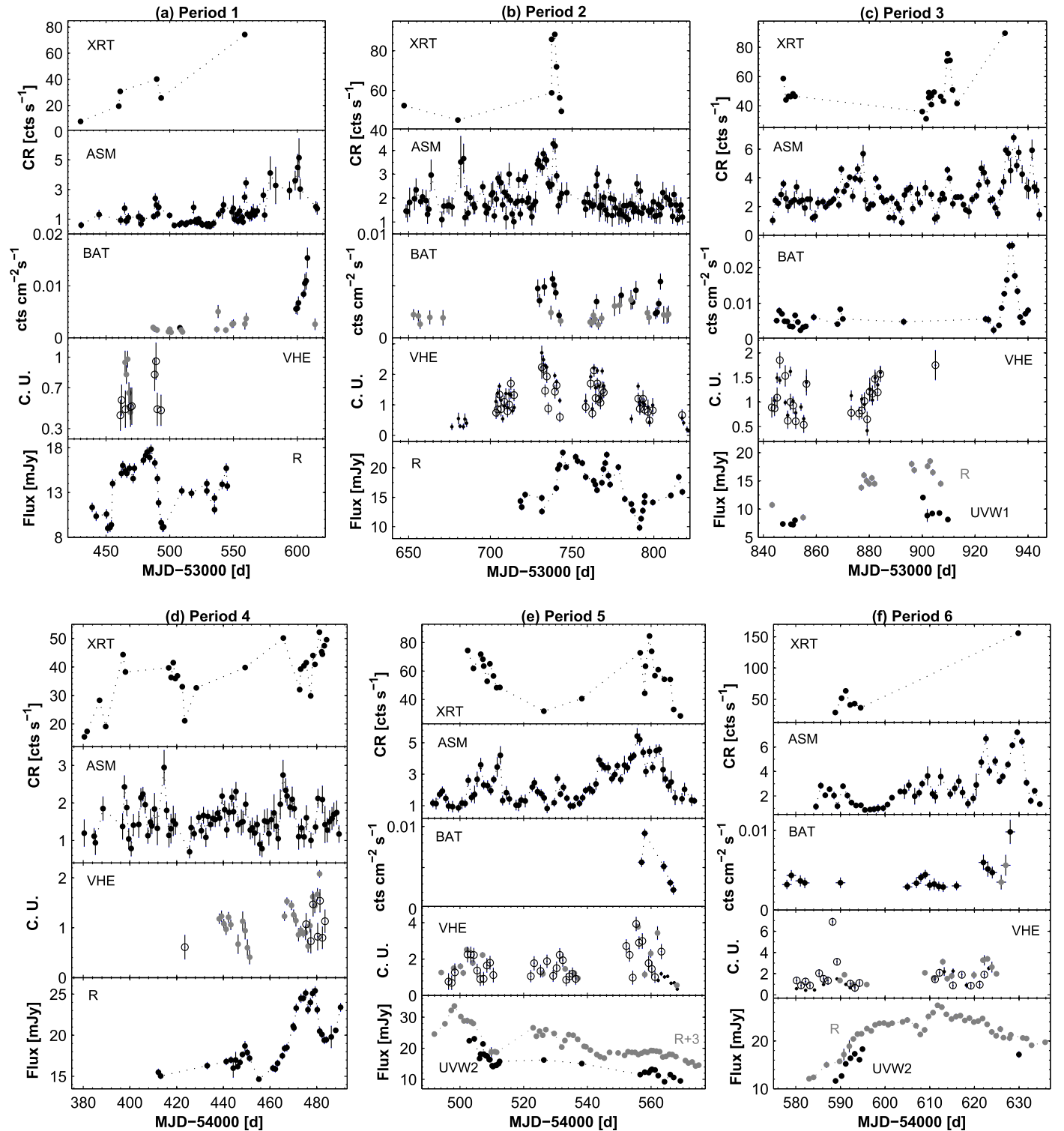


Figure 5. MWL variability of Mrk 421 in different periods (daily-binned data). In the VHE plots, black points correspond to the VERITAS data; gray points and circles represent those from the MAGIC and Whipple observations, respectively. As for the BAT light curves, black and gray points stand for the detections with 5σ and 3σ significances, respectively.

variability and softer values in the time interval containing this peak.

During the densely sampled XRT campaign on 2007 October 24–25 (see Figure 9(b)), the source initially showed a slow variability (a brightening by 40% in 31 ks during ObsID 30352027), while the flux decayed by a factor of 2.2 in 5.6 ks and then increased by a factor of 2.1 in 5.2 ks during

ObsID 30362028. These two extreme events were separated by the 23 ks interval when the source varied relatively weakly. Using the equation $\tau_{d,h} = \Delta t \times \ln(2)/\ln(F_2/F_1)$ (Saito et al. 2013), we obtain the flux doubling and halving times $\tau_{d,h} \approx 1.4$ hr. Note that the flux doubling event was not characterized by a “harder-when-brighter” trend, in contrast to other parts of the observation.

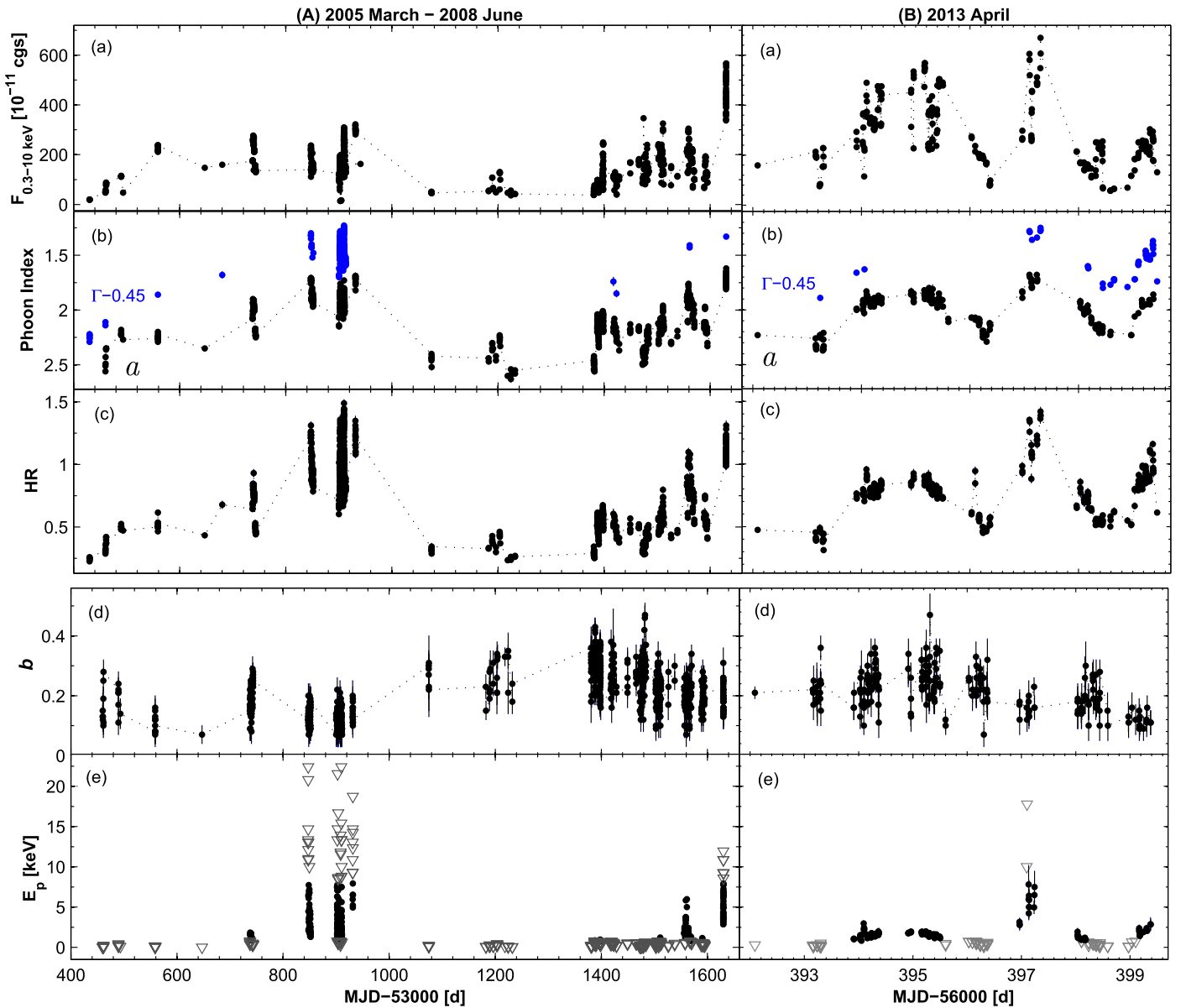


Figure 6. Unabsorbed 0.3–10 keV flux (top panel), photon index (panel (b)), hardness ratio (panel (c)), curvature parameter (panel (d)) and E_p (bottom panel, with gray triangles standing for the values beyond the range 0.8–8.0 keV) plotted vs. time. In the top panel, the acronym “cgs” is a shorthand for for $\text{erg cm}^{-2} \text{s}^{-1}$.

Figure 9(c) presents another run of densely sampled XRT observations performed 2006 April 22–26 when the source initially declined by 39% in 52 ks and exhibited very weak variability during the subsequent 308 ks. In the latter period, the only exception was the first orbit of ObsID 30252006, when the brightness increased by 21% in 1.20 ks. Note that the 0.3–10 keV spectrum, on average, was one of the hardest during 2005–2008 and E_p was always larger than 2 keV.

5. Discussion

5.1. The Position of the Synchrotron SED Peak

Our X-ray spectral study of Mrk 421 has revealed an extreme variability of the parameter E_p during 2005 March–2008 June. In lower X-ray states, the synchrotron SED peak was situated at energies as low as a few tens of eV, while the source was a hard X-ray peaking HBL on 205 occasions (amounting to 24% of all log-parabolic spectra). The latter result is extreme for this

source, and this period was remarkable for the unprecedented high percentage of hard X-ray peaking spectra for Mrk 421. During the strongest X-ray flares in 2013 April, 27 spectra from the XRT observations (13% of all log-parabolic spectra) showed $E_p > 2$ keV with the highest value of 10 keV (see Paper I and Figure 6(Be)), versus $E_p^{\text{max}} = 22.4$ keV in the period presented here (see Figures 6(Ae)–(Be) and Paper I). Although *NuSTAR* observations in the 3–79 keV energy range in 2013 April showed a higher percentage of hard X-ray peaking spectra (19%), the peaks with $E_p \lesssim 3.5$ keV are poorly constrained by the observational data and should be considered as upper limits to the intrinsic value (Paper I). Furthermore, the highest value of E_p from these observation does not exceed 5 keV. As for the period of 2013 November–2015 June, only 28 spectra (5% of all log-parabolic spectra) showed the position of the synchrotron SED peak in hard X-rays and $E_p^{\text{max}} = 9.2$ keV (Paper II).

Table 7
Summary of the 0.3–10 keV IDVs in 2008 March–2008 June

ObsID(s) (1)	Dates (2)	ΔT (hr) (3)	χ_r^2/dof (4)	Bin (5)	$F_{\text{var}}(\%)$ (6)	a or Γ (7)	b (8)	E_p (keV) (9)	HR (10)
35014001	2005 Mar 31	14.75	10.88/34	120 s	6.7(0.4)	2.43(0.02)–2.56(0.03)LP 2.56(0.01)–2.59(0.01)PL	0.13(0.04)–0.15(0.06)	0.02(0.01)–0.03(0.01)	0.29(0.01)–0.36(0.01)
35014002	2005 Apr 01	19.47	12.60/12	120 s	5.9(0.5)	2.35(0.02)–2.36(0.02)	0.10(0.04)–0.28(0.04)	0.03(0.01)–0.24(0.06)	0.37(0.01)–0.42(0.01)
35014006	2005 Jul 07	3.51	2.440/21	120 s	1.3(0.3)	2.20(0.02)–2.29(0.02)LP 2.56(0.01)PL	0.08(0.04)–0.16(0.04)	0.02(0.01)–0.17(0.05)	0.47(0.02)–0.62(0.02)

Note. In Column 1, “Or” stands for “Orbit.” The third column gives the total length of the particular observation (including the intervals between the separate orbits). Columns 7–10 give the ranges of the photon index, curvature parameter, the position of the synchrotron SED peak, and hardness ratio. In Column 7, the acronyms “LP” and “PL” denote log-parabolic and power-law spectra, respectively.

(This table is available in its entirety in machine-readable form.)

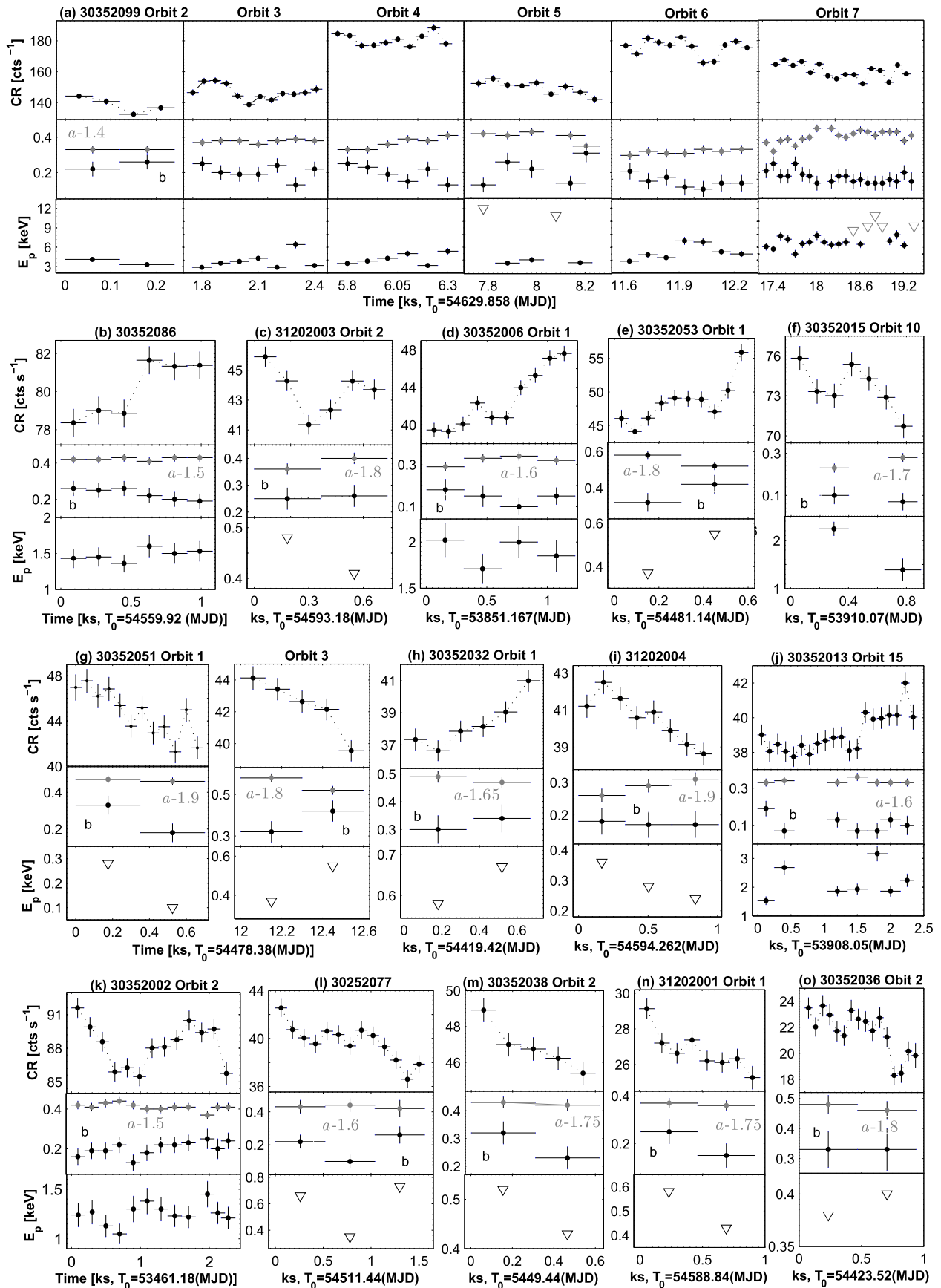


Figure 7. Fastest X-ray IDVs in 2005 November–2008 June. In bottom panels, gray triangles represent the E_p values beyond the range 0.8–8.0 keV.

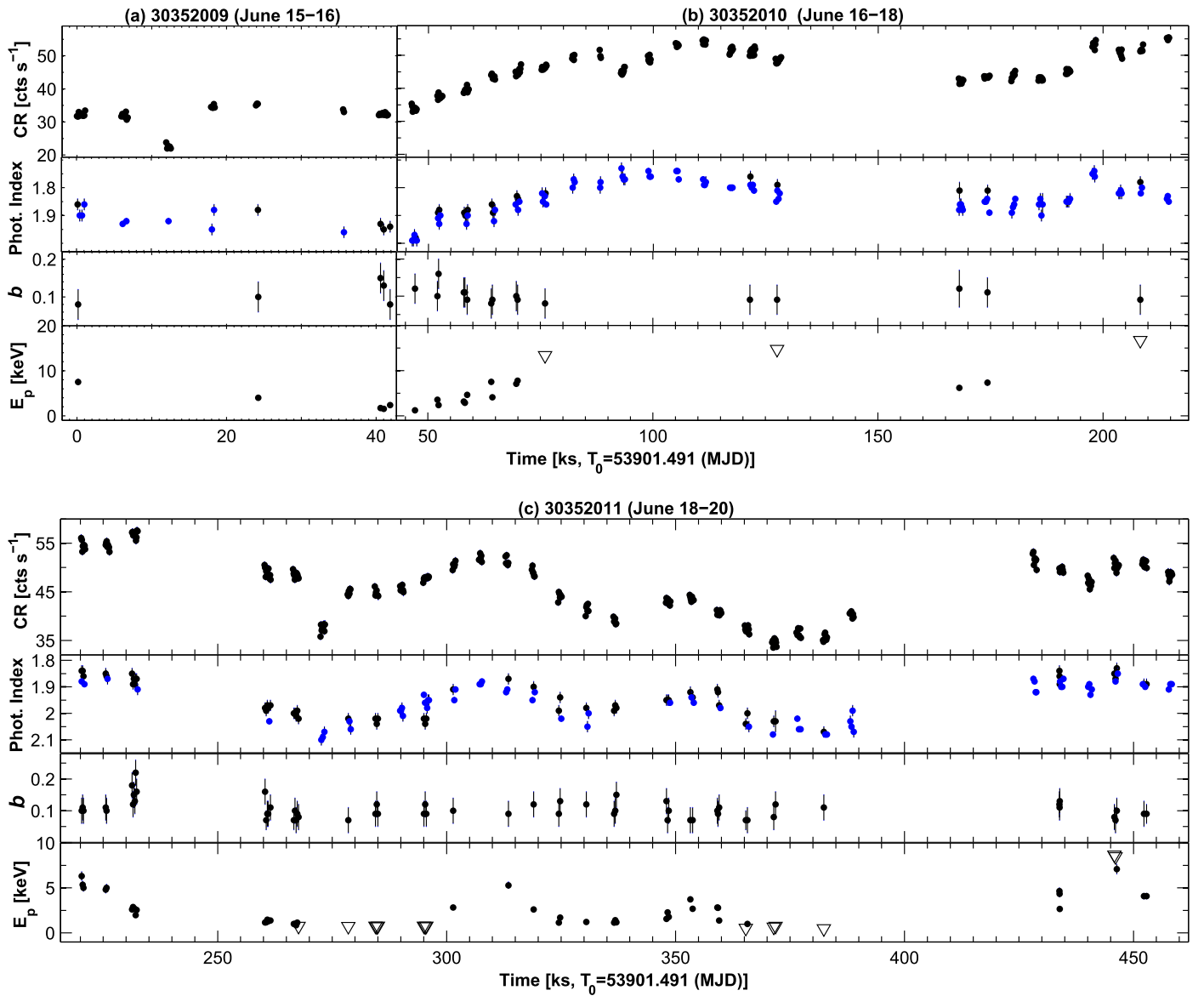


Figure 8. X-ray IDVs from the most densely sampled XRT observations of Mrk 421 in 2006 June (see the next page for Figures 8(d)–(g)). In the second panel of each sub-figure, black and blue points stand for the parameters a and Γ , respectively. In the bottom panels, gray triangles represent the E_p values beyond the range 0.8–8.0 keV.

Note that the largest shifts in E_p toward higher energies and vice versa, reported in Section 4.3, correspond to the shift of ~ 1 order of the frequency, and the overall range of the peak frequency (defined as $\nu_p = E_p/h$) during the whole 2005 March–2008 June $\Delta \log \nu_p \approx 2.5$ orders. However, the variability of E_p in Mrk 421 is less extreme than that exhibited by Mrk 501 during the dramatic X-ray flare in 1997 April when the position of the synchrotron SED moved from 0.94 keV to beyond 100 keV (Pian et al. 1998; Tavecchio et al. 2001). While the presence of the synchrotron peak beyond 100 keV was firmly established during that unprecedented event, it could not be constrained from above due to the insufficient sensitivity of *BeppoSAX* beyond 100 keV (see Tavecchio et al. 2001). Mrk 501 showed a large shift from 0.79 keV to ~ 22 keV, also during the strong X-ray activity in 2014 March–October, observed with XRT. Note that 95% of these spectra showed $E_p > 2$ keV and a distribution peak at ~ 3.5 keV (Kapanadze et al. 2017b), while Mrk 421 exhibited a significantly lower percentage in the aforementioned three

periods when it underwent significantly stronger X-ray flares in those epochs than did Mrk 501 in 2014.

Different investigations of Mrk 421 data still try to understand its strong spectral variability in terms of a single physical process, with (at best) limited success. Namely, the detection of the correlation $S_p \propto E_p^\alpha$ can be used to draw a conclusion about which physical factor makes the main contribution to the observed spectral variability of the source, depending on the values of the exponent α (ranging between 0.60 and 4; Massaro et al. 2008; Tramacere et al. 2011). Figure 10(a), (b), (d) presents a weak positive S_p – E_p correlation during the period 2005 March–2008 June, Periods 2 and 5, respectively, while we observe a medium correlation in Period 3 (Figure 10(c)) and a strong one in Period 6 (Figure 10(e); see Table 4). In the latter case, $\alpha = 0.52 \pm 0.09$, which is close to $\alpha = 0.60$, implying that the main driver of the observed spectral changes is the variability of parameters D_p (the momentum-diffusion coefficient) and q (the exponent describing the turbulence spectrum) during stochastic acceleration of the particles (Tramacere

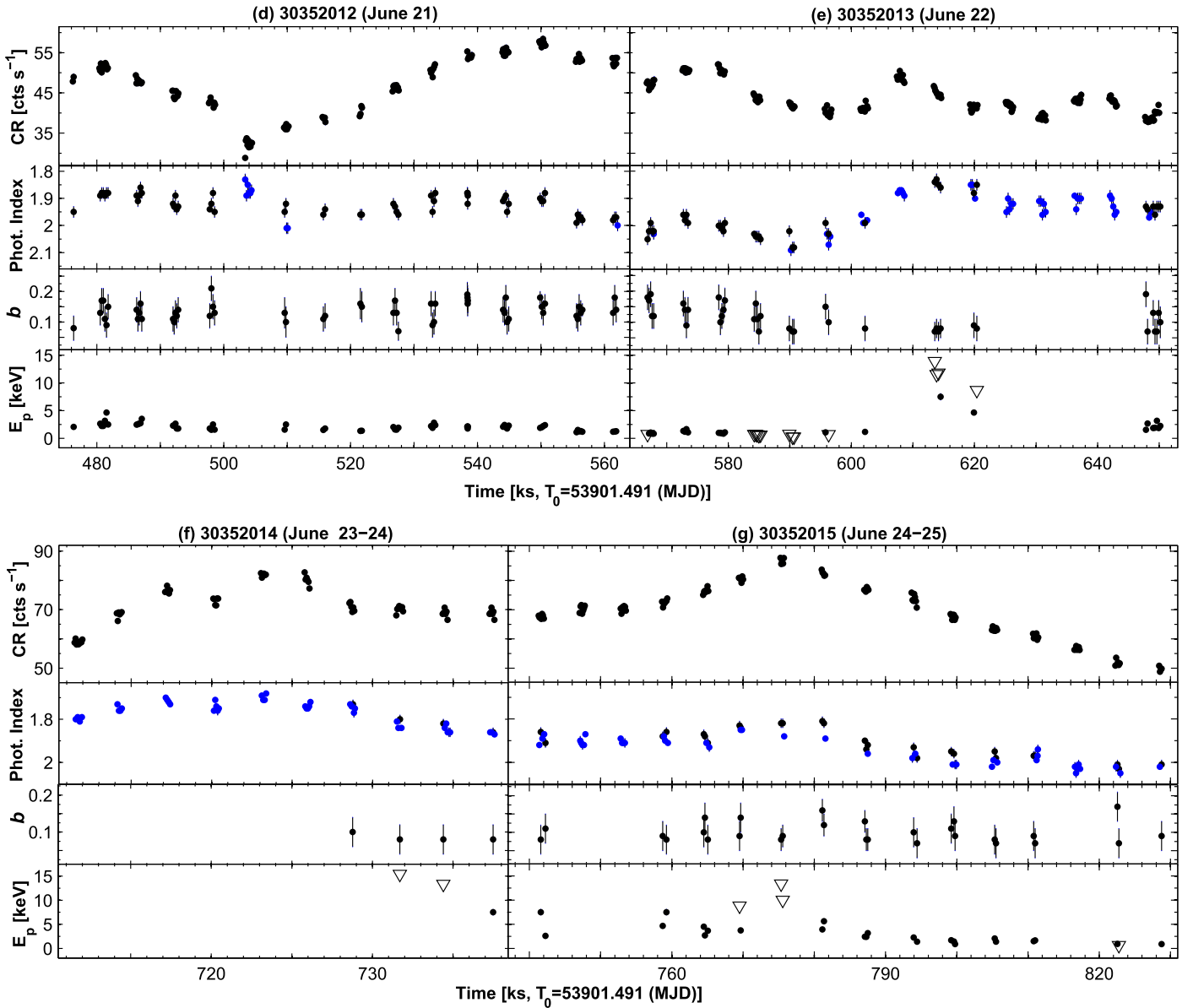


Figure 8. (Continued.)

et al. 2011). Namely, there is a transition from the Kraichnan spectrum ($q = 3/2$) of the turbulence into the “hard sphere” spectrum ($q = 2$) through the Kolmogorov one ($q = 5/3$). In other periods, the exponent showed significantly smaller values ($\alpha \sim 0.25$), leading to the conclusion that the observed strong spectral variations in each one were triggered by the underlying complex and variable physical conditions, with no dominant factor. On the other hand, the aforementioned relation is obtained in the framework of the synchrotron emission mechanism from one dominant homogeneous component that may not be an appropriate assumption for our target in those periods.

5.2. Interband Cross-correlations

5.2.1. Hard versus Soft X-Rays and Spectral Hysteresis

The unabsorbed soft 0.3–2 keV flux showed a strong positive correlation with the hard 2–10 keV flux in all periods, although this correlation was weaker in Period 5 (Table 4).

Figure 2(h) shows that the sub-samples from Periods 3 and 6 (with the most extreme spectral behavior of our target) have different, larger slopes compared to those from other periods, which may hint at different underlying physical conditions.

However, the hard flux varied with a larger amplitude than the soft one in each period (see Table 6 and Figure 11), yielding a strong spectral variability. This difference was especially large in Period 1 when a maximum-to-minimum flux ratio $R = 10.5$ in the 0.3–2 keV flux versus $R = 23.5$ in the 2–10 keV band. For the whole 2005 March–2008 June period, $R = 89.5$ in the 2–10 keV flux, while this quantity was equal to 17.3 in the soft X-rays. Note that both these ratios are significantly larger than their counterparts from the period 2013 November–2015 June and 2013 April.

The difference in the variability of Mrk 421 in the soft and hard X-rays leads to the interesting behavior of the source in the HR–flux plane (so-called spectral hysteresis; Figure 11). On longer-term timescales, it followed clockwise (CW) loops during some intervals of Periods 3–6 (see Figure 11(b)–(f) and

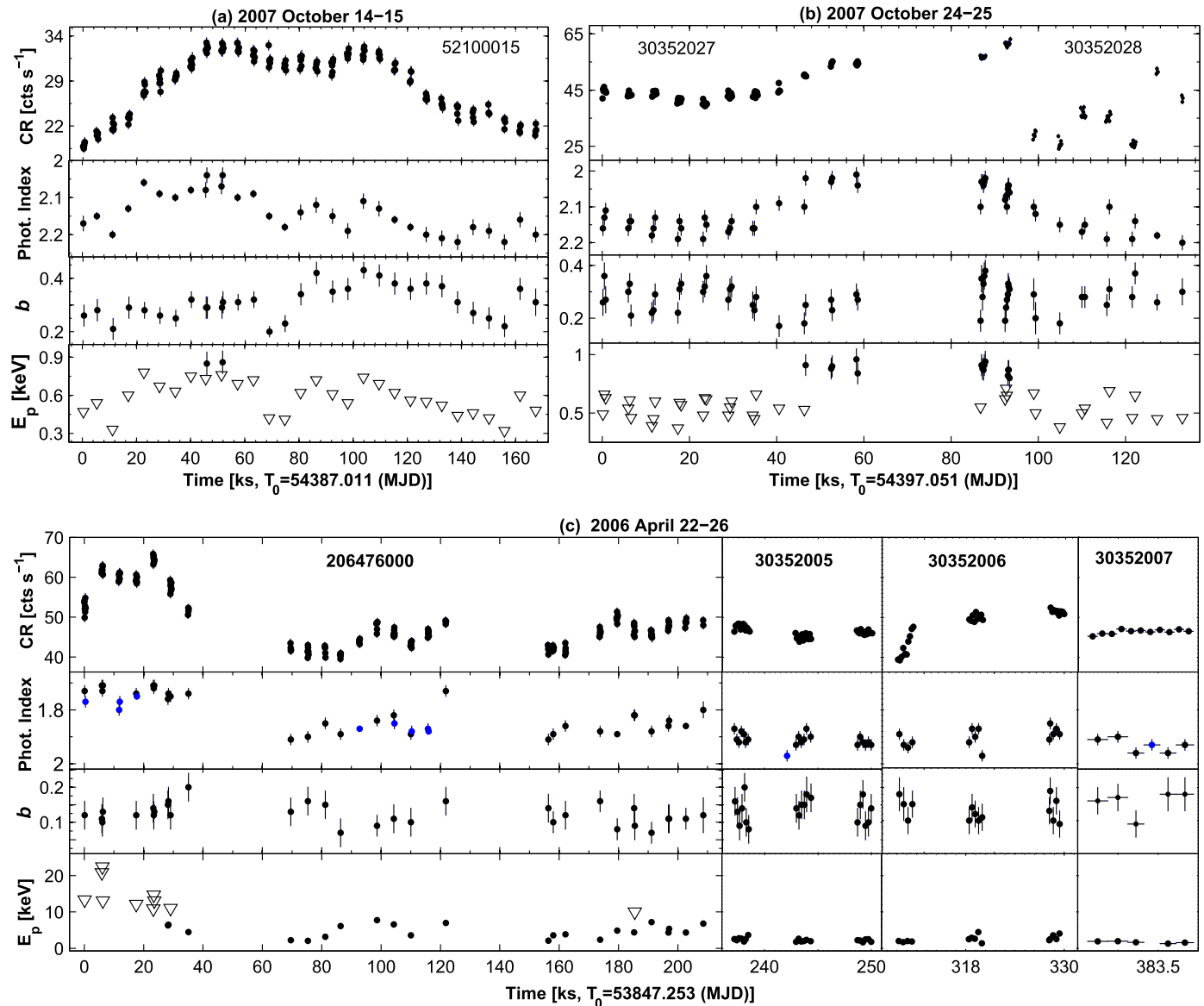


Figure 9. X-ray IDVs from other densely sampled XRT observations of Mrk 421. In the second panels, black and blue points stand for parameters a and Γ , respectively. In bottom panels, gray triangles represent E_p values beyond the range of 0.8–8.0 keV.

Table 8 for details). In the case of the CW-type spectral evolution, the acceleration (τ_{acc}), synchrotron cooling (τ_{syn}), and flux variability (τ_{var}) timescales of the X-ray emitting particles should be related as follows (Cui 2004): $\tau_{\text{syn}} \gg \tau_{\text{var}} \gg \tau_{\text{acc}}$ or $\tau_{\text{syn}} \gg \tau_{\text{acc}} \gg \tau_{\text{var}}$. In that case, the spectral evolution should be due to the flaring component starting in the hard X-ray band, triggered by a rapid injection of very energetic particles rather than by a gradual acceleration (T09). The spectrum is expected to become progressively harder in the brightening phase of the source and softer in the declining phase. Consequently, the hard X-rays’ variability leads that in the soft X-rays both during the increase and the decrease of brightness, resulting in a so-called soft lag (Takahashi et al. 1996). In fact, 0.3–2 keV and 2–10 keV light curves in Figure 11 (lower panels) exhibit possible soft delays at MJD 53901 and MJD 54474, although the XRT observations of Mrk 421 are not suitable for using the local cross-correlation function (LCCF, Max-Moerbeck et al. 2014) to estimate the significances and derive exact values of these delays; the

duration of each observation generally was much shorter than the time intervals between them.

Counterclockwise (CCW) loops were evident during some intervals in Periods 1 and 3–6 (see Figure 11(b)–(f) and Table 8). During the CCW-type spectral evolution, $\tau_{\text{syn}} \approx \tau_{\text{acc}} \approx \tau_{\text{var}}$, the particles are gradually accelerated, while the brightness decline epoch can be dominated by the particle escape effects; therefore, we should observe a hard lag (Ravasio et al. 2004). The corresponding 0.3–2 keV and 2–10 keV light curves show possible hard lags at MJD 54481 and MJD 54562. Note that such spectral evolution can be related to the stochastic acceleration of the particles (see Section 5.3).

Note also that the source showed hysteresis patterns even on intra-day timescales. Namely, it followed CW loops during the 0.3–10 keV IDVs observed during 2006 June 15–25 (see Figure 11(g)–(h) and (k)–(n), and Table 8 for details), April 22–25 (Figure 11(j)) and July 15 (Figure 11(p)), 2007 October 8–15 (Figure 11(i), (o)). The opposite trend was relatively rare

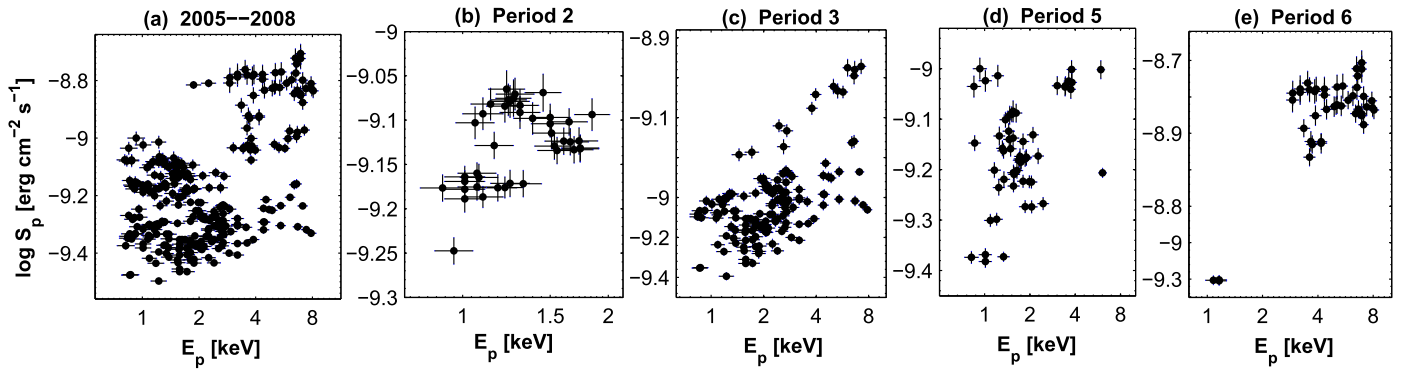


Figure 10. The S_p – E_p relation in different periods.

and observed most clearly on 2006 June 21 (during 19 ks; Figure 11(g)). In other cases, it was not present, or observed during some short intervals on 2006 June 16–18 (Figures 11(h), (l)) and April 22 (Figure 11(j)), 2007 October 14 (Figure 11(i)). No clear trend was evident on 2008 June 12–13, when Mrk 421 showed its highest X-ray state during 2005–2008 (neither during the whole observation, nor during its separate orbits when the source underwent extremely fast IDVs; see Section 4.4.1). Hysteresis patterns on intra-day timescales were also observed during 2013 January–May, and changes from the CW-type evolution into the opposite one within a single observation and vice versa were revealed also in those cases (Paper I). The presence of CW loops was reported by Brinkmann et al. (2001) and Acciari et al. (2009) from *XMM-Newton* observations of our target that were performed in 2000 and 2006, respectively. A similar result was obtained by Takahashi et al. (1996) from the prolonged *ASCA* observation on 1996 May 16/17. No clear patterns were presented on intraday timescales during 2013 November–2015 June (Paper II).

Our study of the hysteresis patterns in Mrk 421 shows various interplays between electron acceleration, synchrotron cooling, and flux variability timescales in 2005–2008 (similar to the 2013–2015 period). A CW trend dominated during Period 3 and a pure CCW trend was evident in Period 1. In other periods (except for Period 2, when no clear loops were evident), CW and CCW trends alternated with each other (even tree-times in turn during Periods 4 and 5). A CW-type evolution was dominant on intra-day timescales, similar to earlier reported findings, and this result hints at the importance of the second-order Fermi process during the fast X-ray variability (see Rebillot et al. 2006). Our HR–flux planes exhibit the cases when the spectrum started to become harder, while the 0.3–10 keV flux was still decreasing, which may indicate the propagation of a new injection from the hard band, as the soft band is still decreasing (T09). The presence of CW or CCW loops and their interchanges on intraday timescales demonstrate that the physical factors responsible for the observed spectral changes varied rapidly in the jet area where the electrons underwent an acceleration to the energies sufficient for the production of X-ray photons.

5.2.2. X-Rays versus VHE and Optical-UV Emissions

Figure 12(a) shows a moderate positive correlation between the 0.3–10 keV and VHE fluxes, while the latter had a relatively weak correlation with the ASM-band flux (see Figure 12(b) and Table 4). As shown in Section 4.2, simultaneous X-ray–TeV flares occurred in all periods

discussed in Section 4. However, the outliers from the general trend in the planes $F_{\text{XRT}}-F_{\text{VHE}}$ and $F_{\text{ASM}}-F_{\text{VHE}}$ hint at uncorrelated X-ray–TeV variability in some epochs. No VHE detections of our target were reported at the end of Period 3 when there was a strong XRT/ASM/BAT-band flare. A similar situation occurred in the first half of Period 4 (two strong flares in the XRT/ASM bands), in Period 5 (the flare around MJD 54512 and 54543 detected with ASM), and Period 6 (around MJD 54630, when the highest 0.3–10 keV and 1.5–12 keV states state in 2005–2008 were recorded). In contrast, the strongest flare, with the highest VHE state during the 3.3 year period presented here, was observed during MJD 55588–55589 (Period 6), when the source showed low X-ray state; however, it was not detected even with 3σ significance in the BAT band.

In the beginning of Period 5, a strong X-ray flare was accompanied by a weaker VHE variability, which is explained by the reduction of the Compton cross-section in the Klein-Nishina regime, strongly suppressing the increase of the flux at highest photon energies (Kataoka et al. 2000).

Uncorrelated X-ray and TeV variabilities in Mrk 421 have been reported by different authors. During the MWL campaign in 2002 December–2003 January, an X-ray flare by a factor of seven was not accompanied by a comparable TeV-counterpart within three days (Rebillot et al. 2006). The TeV flux reached its peak days before the X-ray flux during the giant flare in 2004, which is impossible to explain under the standard one-zone SSC model—Błażejowski et al. (2005) suggested this as an instance of an “orphan” TeV flare. Acciari et al. (2009) did not find a correlation between the simultaneous X-ray–VHE data obtained with *XMM-Newton*, Whipple, and VERITAS in 2006–2008. Several occasions of uncorrelated XRT and VHE variability were observed in 2013 November–2015 June (Paper II): strong, fast VHE flares by factor of 7–13, either without or having non-comparable X-ray brightenings. On the contrary, the source was not detectable or showed a low TeV state during the three X-ray flares—or else there were some shifts between the flares in these bands, which is difficult to explain with the one-zone SSC scenario.

Figure 12(c) presents a positive correlation between the 15–150 keV flux beyond 15 keV (BAT-band) and that below 12 keV (observed with ASM). Contemporaneous flares in these bands were observed in the middle of Period 2, at the end of Periods 3, 5, and 6, and during the second half of Period 4. However, Figure 5 also presents the occasions when the flares beyond 15 keV were not accompanied by a comparable lower-energy flaring activity (at the end of Periods 1–2). On the

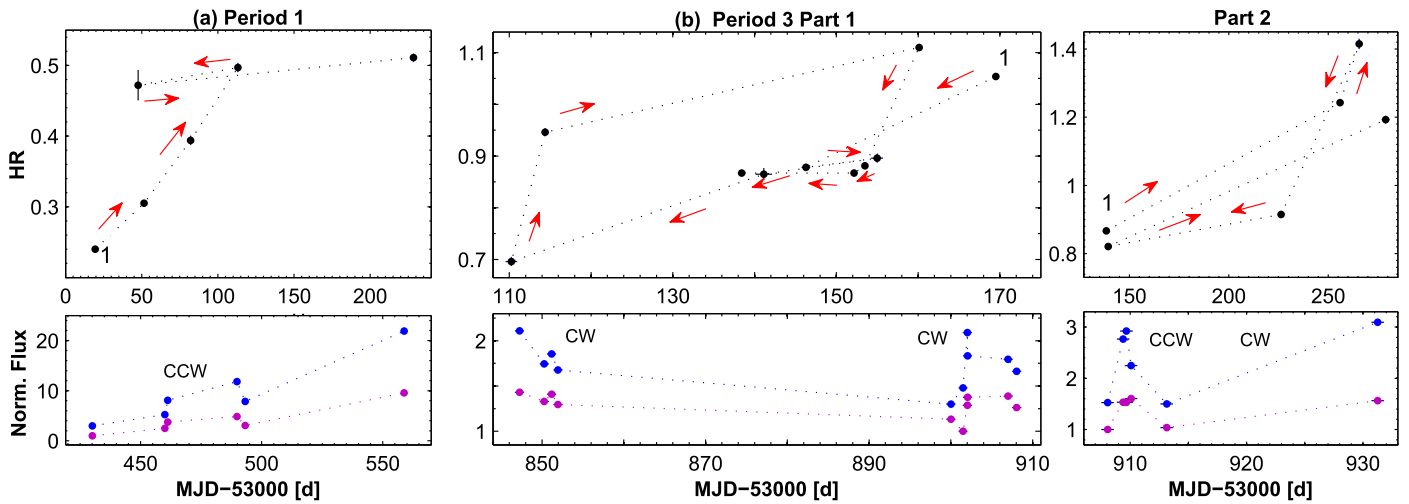


Figure 11. Spectral hysteresis in different epochs, along with the normalized soft 0.3–2 keV (purple points) and hard 2–10 keV (blue points) fluxes plotted as a function of time. The light curves for hard fluxes are shifted arbitrarily for better resolution. In each panel, the start point is denoted by “1.” The acronym “cgs” stands for $\text{erg cm}^{-2} \text{s}^{-1}$.

(The complete figure set (seven images) is available.)

contrary, no BAT detections with 5σ occurred during several ASM-band flares (Periods 3–5). These events suggest either the presence of a separate lepton population producing a flare beyond 15 keV, or that the particles responsible for the lower-energy X-ray flares were not able to produce a flare at higher energies in some epochs.

We have not found a significant correlation between the contemporaneous X-ray and optical-UV observations: Figure 5 demonstrates a mostly “independent” and longer-term optical-UV variability of the source in different periods, with a low state or long-term declining trend along with several X-ray flares. A similar situation was reported by Aleksić et al. (2015a) for Mrk 421 from the MWL campaign in 2009 January–June; those authors explained it as a hardening of the electron energy distribution that can shift the entire synchrotron bump to higher energies. Our finding of a positive E_p –flux correlation (see Section 3.3), i.e., a shift of the synchrotron SED peak location toward higher energies with the increasing X-ray flux, also favors the suggestion of Aleksić et al. (2015a). A similar result was reported also by Tanihata et al. (2004) from the MWL campaign performed for Mrk 421 in 1998 April. Note that the shift of the peak of electron energy distribution with higher brightness was predicted by Katarzyński et al. (2006) in the framework of the stochastic acceleration of electrons with a narrow initial energy distribution, but having an average energy significantly higher than the equilibrium energy. Finally, UV fluxes showed a strong correlation to each other (see Table 4 and Figure 12(d)), and did not exhibit features hinting that they originate from different electron populations.

5.3. Spectral Curvature and Acceleration Processes

The majority of the 0.3–10 keV spectra of Mrk 421 derived from the XRT observations in 2005–2008 were curved. The presence of the spectral curvature and its properties can hint at possible mechanisms that accelerate particles to the energies necessary for the emission of X-ray photons. According to M04, the log-parabolic spectrum of the electrons can be established by the first-order Fermi mechanism at a shock front propagating in a medium where the electrons are confined by a

magnetic field whose confinement efficiency is decreasing with an increasing gyroradius. In that case, the probability p_i of a particle’s subsequent acceleration at step i is related to its Lorentz factor γ_i (i.e., to its energy) as $p_i = g/\gamma_i^q$, where g and q are constants. If $q > 0$, the probability of subsequent acceleration becomes gradually lower as the energy increases, and this may cause the establishment of the log-parabolic electron spectrum (the so-called energy-dependent acceleration probability process; EDAP). In the framework of EDAP, a positive correlation between parameters a and b is expected,¹⁷ but this was the case only for the 0.3–10 keV flares observed in Periods 2 and 3¹⁸ (see Section 4.1). Note that we plotted the chi-squared contours of parameter a versus b for the spectra corresponding to the different X-ray states. Generally, these contours were elongated closely to the direction perpendicular to the overall correlation (see Figure 13, online-only material), demonstrating that the a – b correlation is physical rather than due to the degeneracy. However, these correlations were very weak, hinting at the presence of different acceleration processes (e.g., stochastic mechanism; see below) along with EDAP in these periods. A positive a – b correlation was reported by Kapanadze et al. (2017b) from the XRT observations of our target in 2015 February, and a significantly stronger a – b correlation was reported in M04 from the *BeppoSAX* observations in 1997–1999. Other bright HBLs (1ES 1959+650, Mrk 501, PKS 2155–304) have not exhibited an evidence of EDAP (see Kapanadze et al. 2014, 2016b, 2016c, 2017b, 2017c).

On the other hand, a curved spectral distribution can be established by stochastic acceleration arising from the magnetic turbulence close to the shock front (T09). The simulations of Virtanen & Vainio (2005) showed that the efficiency of the second-order Fermi acceleration may be comparable to that of

¹⁷ See M04 for the details and for the derivation of this correlation.

¹⁸ We checked the presence of the a – b correlation in these periods by selecting higher pivot energies instead of the mutual 1 keV. This change yields practically the same values of the parameter b , while the photon index a shows a systematic shift to higher values and the associated uncertainties increase. Therefore, the positive a – b correlation was observed again in these periods, although it becomes relatively weak due to the presence of larger uncertainties.

Table 8
List of CW and CCW Loops Shown by Mrk 421 in the HR–Flux Plane

Figure	MJD	Variability Event
CW Evolution		
11b, Panel 1	53847.30–53908.12	Low-amplitude flares in the beginning and middle of Period 3 (Figure 5(c))
11b, Panel 2	53910.10–53931.28	Strongest X-ray flare in Period 3 (Figure 5(c))
11c, Panel 1	54398.08–54422.40	High state during the first flare in Period 4 (Figure 5(d))
11c, Panel 2	54472.70–54477.41	Brightness fluctuation during the second flare in Period 4 (Figure 5(d))
11d	54502.40–54510.14	The first flare in Period 5 (Figure 5(e))
11e, Panel 1	54512.52–54538.20	Flux decline and increase between strong flares in Period 5 (Figure 5(e))
11f, Panel 1	54588.76–54592.23	Low-amplitude flare in the start of Period 6 (Figure 5(f))
11g, Panel 2	53907.70–53908.00	IDV on 2006 June 21 (Figure 8(d))
11h, Panel 1	53904.04–53905.33	IDVs during 2006 June 18–19 (Figure 9(c))
11h, Panel 2	53905.69–53905.88	IDV on 2006 June 19 (Figure 8(c))
11h, Panel 2	53906.82–53906.96	IDV on 2006 June 20 (Figure 8(c))
11i	54387.01–54387.00	IDV on 2007 October 14 (Figure 9(a))
11i	54388.50–54388.80	IDV on 2007 October 15 (Figure 9(a))
11j, Panel 1	54847.29–54848.70	IDVs during 2006 April 22–23 (Figure 9(c))
11j, Panel 2	54849.11–54849.90	IDV on 2006 April 23 (Figure 9(c))
11k	53909.41–53909.90	IDVs during 2006 June 23–24 (Figure 8(f))
11l	53902.35–53903.84	IDVs during 2006 June 16–17 (Figure 8(b))
11m	53908.10–50908.50	IDV on 2006 June 22 (Figure 8(e))
11m	53908.60–50908.99	IDV on 2006 June 22 (Figure 8(e))
11n	53910.31–53911.09	IDV during 2006 June 24–25 (Figure 8(g))
11o	54381.70–54382.00	IDV on 2007 October 8
11p	53931.29–53931.60	IDV on 2007 July 15
CCW Evolution		
11a	53430.11–53559.42	Strong X-ray flare in Period 1 (Figure 5(a))
11b, Panel 2	53908.12–53910.10	Fast X-ray flare in the middle of Period 3 (Figure 5(c))
11c, Panel 1	54381.50–54398.08	Brightness increase during the first flare in Period 4 (Figure 5(d))
11c, Panel 2	54422.40–54465.67	Decline after the first flare and the second flare in Period 4 (Figure 5(d))
11c, Panel 3	54477.41–54482.38	Fast minor flare superimposed on the second flare in Period 4 (Figure 5(d))
11d	54510.14–54512.52	Fast minor flare superimposed on the second first in Period 5 (Figure 5(e))
11e, Panels 1–2	54556.60–54569.21	The second strong flare in Period 5 (Figure 5(e))
11f, Panels 1–2	54593.20–54629.82	Strong flare in Period 6 (Figure 5(f))
11g, Panel 2	53907.00–53905.70	IDV on 2006 June 21 (Figure 8(d))
11h, Panel 2	53905.33–53905.69	IDV on 2006 June 19 (Figure 8(c))
11h, Panel 2	53906.55–53906.82	IDV on 2006 June 20 (Figure 8(c))
12i	54388.00–54388.50	IDV on 2007 October 15 (Figure 9(a))
11j, Panel 2	54848.70–54849.11	IDV during 2006 April 23–24 (Figure 9(c))
11l	53902.09–53902.35	IDV on 2006 June 16 (Figure 8(b))

the shock acceleration. Massaro et al. (2011) demonstrated that the electrons in the jets of TeV-detected HBLs should undergo a more efficient stochastic acceleration than in those of the TeV-undetected HBLs, and the synchrotron SEDs are expected to be relatively broad (i.e., to have small values of the parameter b). As we have shown in Section 3.1, the source mostly exhibited a low curvature and showed an anticorrelation with the parameter E_p , as expected in the case of effective stochastic acceleration—showing that spectral curvature is related to the acceleration, rather than to the cooling process (T09). However, the latter was weak (or very weak) in different periods, which can be explained as due to “contamination” of a stochastic acceleration of the electrons by cooling and other types of acceleration processes (Kapanadze et al. 2016c).

Note also that the source showed an unprecedentedly large percentage of power-law spectra in 2005–2008. As noted above, this period showed the importance of the EDAP (first-order Fermi process), although the parameter q should be not dependent on the particle’s energy in some cases (necessary for the efficient EDAP), leading to the establishment of the

power-law energy distribution of X-ray emitting electrons (see M04). On the other hand, this distribution can be related to fact that the turbulent magnetic field was not sufficiently strong for efficient second-order Fermi acceleration. This means that the properties of the magnetic field in the jet of Mrk 421 were variable in 2005–2008, and sometimes it was not characterized by confinement efficiency decreasing with a rising particle’s energy. Our results also show that the magnetic field properties sometimes were rapidly variable within the jet emission zone: the source showed a transition from a log-parabolic spectrum into a power-law one, and vice versa, within 1 ks observational runs (see Section 3.4).

Our detailed spectral study of Mrk 421 also has revealed an anti-correlation between the spectral curvature and 0.3–10 keV flux, which implies that the source, on average, showed smaller curvatures (i.e., wider synchrotron SEDs related to a more efficient stochastic acceleration) during X-ray flares than in lower states. This result leads to the suggestion that the stochastic acceleration probably was more efficient in the jet during X-ray flares than in other epochs. According to the

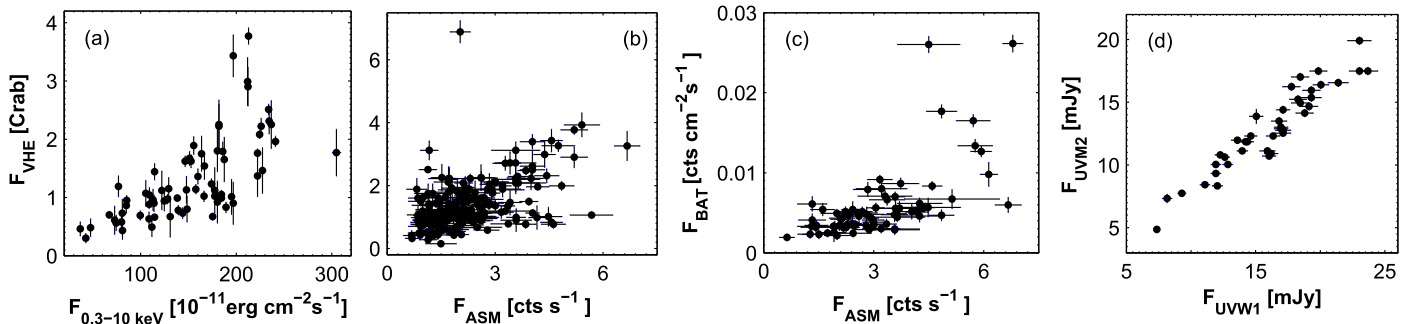
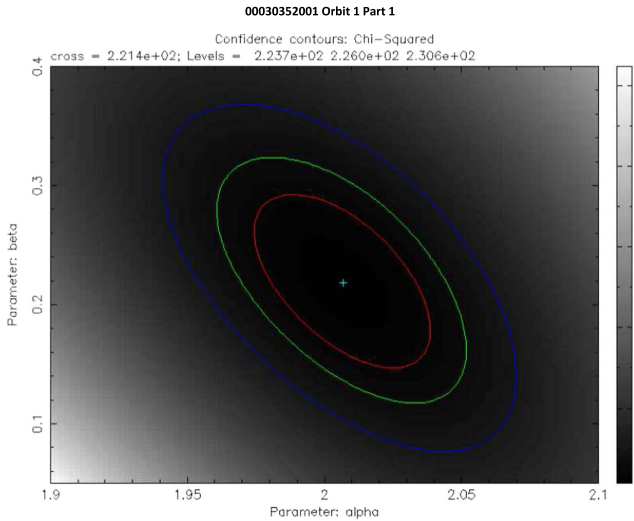


Figure 12. Correlation between the MWL fluxes.

Figure 13. Chi-squared contours of parameter a vs. b for the spectra corresponding to the different X-ray states.

(The complete figure set (eight images) is available.)

shock-in-jet scenario, longer-term blazar flares can be related to the propagation of a shock moving down the jet (Sokolov et al. 2004). The relativistic magnetohydrodynamic simulations of Mizuno et al. (2014) showed that shock propagation through an inhomogeneous medium can yield an amplification of the turbulent magnetic field in a shocked medium, due to its interaction with higher-density inhomogeneities existing in the pre-shock medium. Eventually, the amplification of the jet turbulence can make the second-order Fermi mechanism more efficient. Our discovery of possibly more efficient stochastic acceleration during the flaring states is in favor of these scenarios.

However, the b - $E_{0.3-10\text{ keV}}$ correlation was weak or not observed in all periods discussed in Section 4.2, which hints at the presence of other types of the acceleration mechanisms (e.g., EDAP) not yielding wide SEDs. Such complex acceleration is expected in the scenario presented in Katarzyński et al. (2006): initially, the particle can be efficiently accelerated at the shock front. After escaping into the shock downstream region, the particle is still accelerated by the stochastic mechanism. As a result, the particle energy may increase enough to let the particle re-enter the shock acceleration region and repeat an acceleration cycle by the first- and second-order Fermi mechanisms.

Similar to Mrk 421, low spectral curvatures were found for Mrk 501 during the prolonged flaring activity in

2014 March–October (Kapanadze et al. 2017b). As for other bright HBLs, they generally showed larger curvatures compared to our target (Kapanadze et al. 2014, 2016c, 2017c). The difference was especially conspicuous in the case of 1ES 1959+650 in 2015 August–2016 January, when the majority of the spectra yielded $b > 0.40$ with several values larger than 0.70 (Kapanadze et al. 2016b; the value never shown by Mrk 421).

Mastichiadis & Moraitis (2008) showed that the electrons need an acceleration time of hours in order to attain energies corresponding to the Lorentz factor $\gamma \sim 10^6$ during the gradual acceleration. This timescale can be very long for the first-order mechanism (EDAP), but it matches with the stochastic acceleration timescale within reasonable ranges of different physical parameters (Tammy & Duffy 1992). Note that the simulations of Virtanen & Vainio (2005) showed that the stochastic acceleration in relativistic shocks showed a gradual shift of the whole particle spectrum to higher energies as the particles were accelerated behind a shock front. The predictions of Mastichiadis & Moraitis (2008) are in accord with another of our results—the dominance of a CW-type spectral evolution during the fast variability (0.3–10 keV IDVs; see Section 5.2.1).

5.4. Photon Index and Hardness Ratio

An extreme spectral variability of our target in 2005–2008 was reflected in a very wide range of the photon index. In the low X-ray states, the log-parabolic spectra were very soft, with the photon index at 1 keV exhibiting a maximum value $a = 2.63$. Note that the source showed even softer 0.3–10 keV spectra during 2013 January–2015 June, with a_{max} amounting to 2.83 (Papers I–II). On the other hand, the source exhibited harder spectra than during the giant X-ray flare: the hardest spectrum yielded $a = 1.68$ and HR = 1.31 in the latter case (Paper I), while there were several spectra with $a = 1.62$ – 1.67 and HR = 1.32–1.49 in 2005–2008. Even harder spectra with $a = 1.34$ – 1.45 were reported by Ravasio et al. (2004) from the two *XMM-Newton* observations on 2002 November 4, although a log-parabolic fit yielding $a = 1.16$ – 1.50 for another two spectra (from 2002 November 14 and December 1 observations) gave unacceptable values of χ_r^2 . The source also showed very hard spectra and wide range of parameter a during the *BeppoSAX* observations of 1997–2000 ($a = 1.70$ – 2.54 ; M04).

On the other hand, more extreme results were reported for 1ES 1959+650, with 88–95% of spectra harder than $a = 2$ and 22 spectra with $a = 1.46$ – 1.61 (i.e., harder than those from our study) in the epochs of strong X-ray flares observed during 2016 August–2017 January and 2016 June–August (Kapanadze

et al. 2016b, 2017c). Out of 154 curved spectra of Mrk 501 during 2014 March–October, 153 showed $a < 2$, and 36 spectra out of those 153 yielded $a = 1.39$ – 1.61 (Kapanadze et al. 2017b). Note that our target showed spectra harder than $a = 1.70$ significantly more rarely than Mrk 501 and 1ES 1959+650 in the aforementioned periods. Such very hard spectra are expected in the framework of hadronic models rather than within the one-zone SSC scenario (see Mannheim 1993; Shukla et al. 2015). This result may hint at the possibility of fewer hadronic contributions to the jet matter of Mrk 421 than in Mrk 501 and 1ES 1959+650. Note that the latter source is more prominent with uncorrelated X-ray—VHE variability and “orphan” TeV flares (see Krawczynski et al. 2004; Kapanadze et al. 2016b, 2017c) than our target, and the uncorrelated variability is “tolerated” by hadronic models (see, e.g., so-called synchrotron proton blazar model; Abdo et al. 2011), in contrast to one-zone SSC scenarios.

As for the power-law spectra, the source exhibited a range of the 0.3–10 keV photon index $\Gamma = 1.68$ – 2.74 in 2005–2008, and practically the same range was shown in 2013 January–May (Paper I). However, there was a significantly higher percentage of power-law spectra in the former period (28% versus 13%), while they were observed rarely in 2013 November–2015 June (5%; Paper II). Source 1ES 1959+650 also showed a very uneven percentage of power-law spectra in different epochs: it amounted to 16% in 2017 January–August (Kapanadze et al. 2017c) against 2% in 2005–2014 and only one occasion in 2015 August–2016 January (Kapanadze et al. 2016b, 2016c). We therefore conclude that the physical conditions in HBL jets are not equally suitable for the generation of a power-law energy spectrum of the X-ray emitting particles in different epochs.

A good fit of the most of these spectra with the power-law model cannot be simply related to the possible case when the presence of the synchrotron SED peak position far beyond the XRT instrumental range can make difficult to evaluate the spectral curvature in the 0.3–10 keV energy range (see Massaro et al. 2008): the log-parabolic spectra showed comparable hardness ratios in those epochs when the power-law spectra were observed. Nevertheless, the source showed an anti-correlation between the curvature parameter and the X-ray brightness; i.e., on average, the farther the SED peak position from the lower energy bound of XRT, the higher the spectral curvature was. However, for the XRT observation performed on 2006 June 23 (MJD 53909), yielding values $HR > 1.35$ for the power-law spectra (i.e., harder than the hardest log-parabolic spectra), T09 performed a joint XRT-BAT spectral analysis and found a significant spectral curvature with $b = 0.13 \pm 0.02$ and $E_p = 34^{+22}_{-11}$ keV; i.e., the non-detection of significant curvature from the XRT data alone was related to the presence of the synchrotron SED peak location far beyond the instrumental range of this telescope. A similar situation was found for the power-law spectra from the 2006 April 22 observation (MJD 53847; Orbits 1–4 of MJD 206476000), which yielded a significant curvature with $b = 0.11$ – 0.13 and $E_p = 20^{+10}_{-6} - 26^{+19}_{-8}$ keV in the case of the joint XRT-BAT spectral analysis.

In the period presented here, the source showed an unprecedentedly high percentage of spectra with $HR \geq 1$ (26%), i.e., those with higher hard 2–10 keV flux compared to the soft 0.3–10 keV flux. Note that such spectra were observed in flaring X-ray states of Mrk 421, and this result is unusual for HBL

sources where the contribution of X-ray photons of the IC origin in the 0.3–10 keV energy range is not expected in higher X-ray states, in contrast to the LBL sources. The spectra with $HR \geq 1$ were observed significantly more rarely in 2013 April and 2013 November–2015 June (8% of all spectra in each period; see Figures 6(Ac)–6(Bc)). In the latter period, the source followed a “harder-when-brighter” trend during spectral variability that was stronger than in 2005–2008: the correlation coefficient between HR and $F_{0.3-10 \text{ keV}}$ amounted to 0.64 and 0.53, respectively. This result is partially related to the fact that the sub-sample corresponding to the strongest flare in 2008 June showed an opposite trend (see Sections 3.2 and 3.4). Note that the source showed a “softer-when-brighter” trend also for the sub-sample from the 2014 January–February observations of our target (Paper II). The same trend was seen within some short intervals during the very intense XRT campaign performed in 2006 June (see Section 4.4.2). This trend can be related to the consecutive emergence of soft X-ray components in the X-ray emission zone resulting in a brightness increase while softening the observed 0.3–10 keV spectrum.

5.5. Flux Variability

5.5.1. Variability Amplitudes

During the 3.3 year period presented here, Mrk 421 showed a strong X-ray flaring activity, by a factor of 2–10, on timescales of few days to weeks, and a maximum-to-minimum flux ratio of 20 and 15 in the XRT and ASM bands, respectively. However, this range could be significantly larger in the ASM band because the source’s detection in the lower states was restricted by the limited instrumental capabilities. The 0.3–10 keV count rate exceeded the threshold of 100 cts s^{-1} for the first time since the start of *Swift* observations on 2008 June 12, and attained a value of 155.6 cts s^{-1} (corresponding to 5.7×10^{-9} erg cm^{-2} s^{-1}). Comparable or higher brightness states were observed only during the giant X-ray flare in 2013 April (see Figure 6(Aa), (Ba)). In contrast to the latter, the source was observed only once with XRT in 2008 June, and it was monitored intensively only within some restricted intervals during both the 2006 April and 2006 June flares (the epochs of the most extreme spectral behavior). Therefore, the details of these extreme flares are unknown. Although the contemporaneous ASM observations exhibit a very strong flare in the 1.5–12 keV energy range, comparable flares were also observed with this instrument in 2006 and 2010, in contrast to the XRT band.

Due to the extreme position of the synchrotron SED peak location in 2006 April–June, the source then showed its strongest 15–150 keV flare; an unprecedented number of detections with 5σ significance during 2005–2016 occurred in this epoch. This flare was significantly stronger than those recorded along with the strongest X-ray flares in 2008 June and 2013 April.

In the $\log \nu - F_{\text{var}}$ plane, where the F_{var} values from each band are calculated using all the available data obtained with various instruments during 2005–2016, Mrk 421 shows a double-peaked shape with the highest variability in the X-ray and VHE bands (Figure 14(a)). In each band, daily binned data are used to calculate F_{var} , except for the 0.3–300 GeV energy range where the one-week binned data obtained with the Large Arc Telescope (LAT) onboard the satellite *Fermi* (Atwood et al. 2009). A similar shape is evident in Figure 14(b), (c)

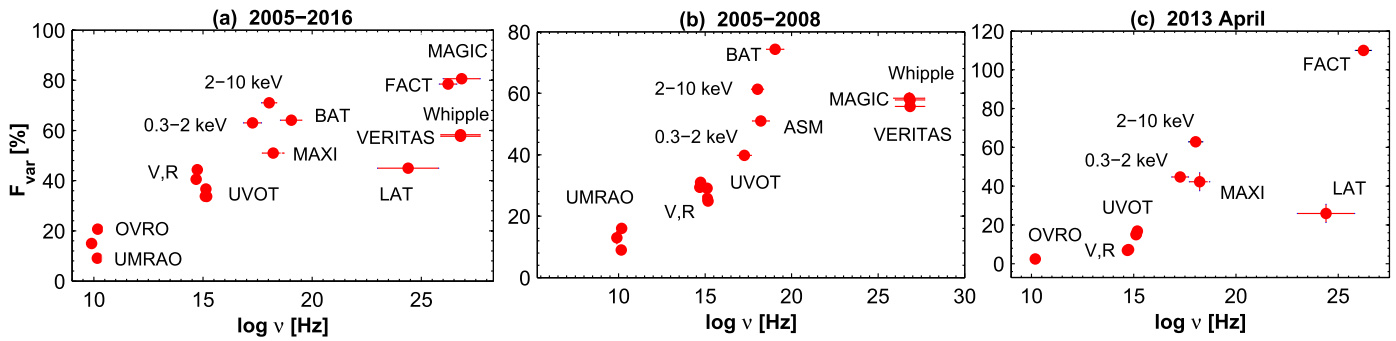


Figure 14. F_{var} as a function of the energy in different periods.

where a $\log \nu - F_{\text{var}}$ plot is constructed separately for the periods 2005–2008 and 2013 April. In the latter case, the 2D binned LAT fluxes are used to derive the fractional amplitude. Note that the value of F_{var} is known to be dependent on the data sampling, and the use of larger time bins in the LAT band (due to limited sensitivity) could underestimate F_{var} . For the calculation of fractional amplitudes from observations performed with the 26 m telescope of University of Michigan Radio Astronomy Observatory (UMRAO; 4.8–14.5 GHz frequencies; Aller et al. 1985), Owens Valley Radio Observatory¹⁹ (OVRO, 15 GHz; Richards et al. 2011), ASM, MAXI satellite²⁰ (Matsuoka et al. 2009), BAT, Whipple, VERITAS, MAGIC, and First G-APD Cherenkov Telescope (FACT; Anderhub et al. 2013), we used only the flux values from those time bins when the source was detected with 3σ – 5σ significances. Therefore, the aforementioned two-humped shape in the $\log \nu - F_{\text{var}}$ should be treated with caution. Note also that the F_{var} value from the BAT observations is larger than that from the whole 2005–2016 period. This result could be related to fact that the position of the synchrotron SED peak was observed significantly more frequently in 2005–2008 than during 2009–2016.

A double-humped shape in the $\log \nu - F_{\text{var}}$ plane, exhibiting the highest variability in the X-ray and VHE bands, was interpreted by Furniss et al. (2015) as resulting from a correlation between the synchrotron and IC peaks, and it provides an indication that the electron energy distribution is most variable at the highest energies (see Aleksić et al. 2015b). Although a limited sensitivity and the use of larger time bins can underestimate F_{var} values for some instruments, a double-peak shape in the $\log \nu - F_{\text{var}}$ plane seems to be inherent for HBLs, and it has been reported by various authors for Mrk 421 from the MWL campaign performed in various epochs (Paper I, Aleksić et al. 2015b; Ahnen et al. 2016; Baloković et al. 2016), for Mrk 501 in 2014 March–October (Kapanadze et al. 2017b), and for 1ES 1959+650 in different epochs (Kapanadze et al. 2016c, 2017c).

5.5.2. Flux Variability on Intra-day Timescales

Our target was very active also on intra-day timescales, and the corresponding duty cycle (DC, Romero et al. 1999), the fraction of total observation time during which the object displayed 0.3–10 keV IDVs, was 84%; i.e., it was practically the same as in 2013 January–May (Paper I), while the DC was only 46% in 2013 November–2015 June. However, this result

can be partially related to significantly less densely sampled observations in the latter period. Mrk 421 was a target during the exposure of 119 ks distributed over 124 XRT orbits within a period lasting 830 ks (including the intervals between the orbits or subsequent observations) in 2006 June 15–25 (see Figure 8). This was a density of observations unprecedented since the start of blazar monitoring with *Swift*, and it was more intense than that carried out during the giant flare in 2013 April 10–17. The source was also targeted very frequently during some other time intervals of 2005 March–2008 April presented in Figure 9. As for the period 2013 November–2015 June, the densest samplings amounted only to 7.3–9.6 ks, distributed over 7–8 orbits within 36–294 ks.

Figure 15 presents the quantity f_{var} as a function the flux for the 0.3–10 keV IDVs that occurred in Mrk 421 in different periods. We see that the majority of these events in the period presented here (the first panel) occurred during higher X-ray states, and a similar situation was observed during the giant flare in our target (second panel). However, the majority of the 0.3–10 keV IDVs occurred in lower states during the period 2013 November–2014 May, and the highest values of f_{var} were recorded in these states (last panel), in contrast to the former two periods. The IDVs observed during the flaring epochs favor the shock-in-jet scenario (interaction of a propagating shock front with jet inhomogeneities; Sokolov et al. 2004). IDVs caused by other mechanisms occurring in the innermost blazar area should be more conspicuous when the source is relatively faint, i.e., the variable emission from the black hole vicinity will not be overwhelmed by the huge amount of the flux produced near the shock front (see, e.g., Kapanadze et al. 2014, 2016a, 2016c). We conclude that the importance of the flow disturbances occurring in the innermost AGN region and triggering 0.3–10 keV IDVs could be higher in 2013 November–2014 May, while a shock interaction with jet inhomogeneities could be the dominant process producing 0.3–10 keV IDVs in the period presented here and in 2013 April.

Similar to the periods 2013 January–May and 2013 November–2015 June, Mrk 421 showed rapid flux changes within 1 ks observational runs in 2005–2008: brightness increases by 4–19% within 180–900 s and declines by 4–20% within 180–960 s. Note that these instances mostly were observed in higher X-ray states and this result also is in favor of the shock-in-jet scenario: shock propagation can strongly amplify the turbulence in the shocked jet material (as discussed in Section 5.3). The higher-energy photons (including those having 0.3–10 keV energies) are expected to originate in the smallest areas, which contain the strongest magnetic field, yielding the most rapid time variability (see

¹⁹ <http://www.astro.caltech.edu/ovroblazars/>

²⁰ Retrieved from <http://maxi.riken.jp/>.

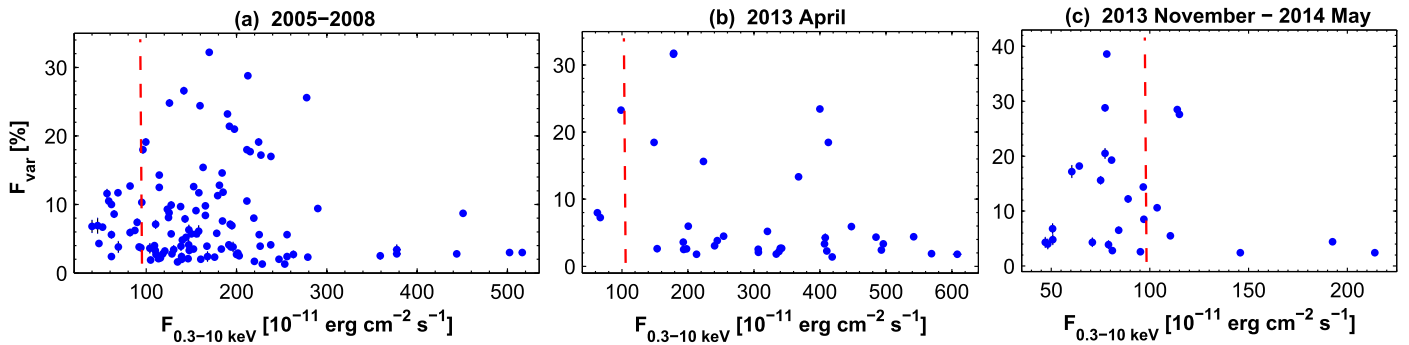


Figure 15. F_{var} values of the 0.3–10 keV IDVs plotted vs. flux in different periods. The vertical, red dashed lines represent the mean weighted value of the 0.3–10 keV flux during 2005–2015.

Mizuno et al. 2014). Although two very fast IDVs in Figure 7 are observed at relatively lower brightness states (corresponding to 21–29 cts s^{-1}) compared to other instances presented in the same figure, they belong to the epochs of X-ray flares in the first half of Periods 4 and 6. Nevertheless, these states are significantly higher than those shown by Mrk 421 during the densely sampled XRT observations performed in the quiescent states in 2005–2016 (corresponding to $\text{CR} \lesssim 10 \text{ cts s}^{-1}$; see Figure 4(a)).

The densely sampled XRT observations, performed in 2005–2008, show that the source exhibited an unequal activity in different time intervals on intra-day timescales: it varied only by 13–54% within 24–82 ks and did not even show a flux variability at the 3σ confidence level during 18–65 ks (see Figures 8–9), while the same observations showed the fastest flux doubling/halving times of about 1.4 hr and the source underwent rapid IDVs for a few hundred seconds. Note that Mrk 421 showed more than 15 flux doubling/halving instances on intraday timescales (versus two instances in 2005–2008) with shorter doubling and halving times on some occasions (about 1.0 hr and 1.2 hr, respectively). Their amplitudes were also larger compared to those observed in the period presented here: while the strongest IDV was related to the flux increase by a factor of 2.1 in 2005–2008, the source showed several brightenings by a factor of 2.4–8.8 in 2008 April. Moreover, the source did not exhibit the intervals with non-variability or slow variability during the densely sampled observations XRT and *NuSTAR* performed in that period, in contrast in the period presented here. A stronger variability of Mrk 421 on intraday timescales in 2013 April could be related to more highly developed turbulence (according to Mizuno et al. 2014 and Sokolov et al. 2004) which, in turn, possibly was established after the propagation of a significantly stronger shock through jet that yielded a giant flare with significantly higher X-ray states than those observed in 2005–2008.

Along with the 0.3–10 keV flux, different spectral parameters showed variability on intraday timescales. Sometimes these variations occurred even within 1 ks observational runs, and these events were related to the IDVs presented in Section 4.4.1. Namely, the spectrum softened by $\Delta a = 0.08\text{--}0.10$ in 400–500 s and hardened by $\Delta a = 0.07$ in 330 s. In the case of the SED peaks, which are well-constrained by the XRT data, the most extreme variability was a shift by 1.2–3.2 keV toward higher energies in 400–600 s. These instances should be related to the rapid changes in the energy distribution of X-ray emitting particles and underlying physical conditions in the jet-emission zone. The source showed similar rapid events also in 2013 April (Paper I),

while the spectral changes were less extreme during 2013 November–2015 June, and only one occasion of the intra-hour variability was recorded (see Paper II).

6. Conclusions

In this paper, we have presented the results of a detailed spectral study of nearby TeV-detected blazar Mrk 421, based on the rich archival data obtained with *Swift*-XRT during 2005 March–2008 June. This period was characterized by the dominance of log-parabolic spectra, although we obtained a significantly higher percentage of the power-law spectra (28%) compared to other periods (5–13%). The E_p parameter showed a positive correlation with the 0.3–10 keV flux: during strong X-ray flares, the position of the synchrotron SED peak of 41 log-parabolic spectra were found beyond 8 keV, with considerably higher lower limits to E_p than during the giant X-ray flare in 2013 April. On the other hand, the position of the synchrotron SED peak sometimes shifted to energies as low as a few tens of eV in quiescent states. In the case of 24% of all log-parabolic spectra, Mrk 421 was a hard X-ray peaking HBL source. In the case of the SED peaks well-constrained by observational data, they showed rapid shifts by 1.2–3.2 keV toward higher energies in 400–600 s. The sample of the spectra from the period 2008 April–June showed a relation $S_p \propto E_p^{0.6}$, as expected in the case of variable momentum-diffusion coefficient and turbulence spectrum (a transition from the Kraichnan into the hard-sphere one). Strong spectral variations in other periods indicate the presence of complex and variable underlying physical conditions, with no dominant factor.

The source mostly showed low spectral curvature during 2005–2008, as expected in the case of efficient stochastic acceleration in the jet of Mrk 421. The viability of the second-order Fermi mechanism is corroborated by the observed E_p – b anti-correlation, although the weakness of the latter and the presence of the a – b correlation in some periods leads us to the suggestion that both Fermi mechanisms could be at work in the jet of our target. This possibility is in agreement with the previous theoretical studies yielding a consecutive shock and stochastic accelerations of particles in the jets of TeV-detected blazars.

In the period presented here, the photon index at 1 keV exhibited a broad range of the values, and several times it was smaller than in 2013 April ($a = 1.62\text{--}1.67$). The 0.3–10 keV photon index from the power-law spectra also showed a broad range ($\Gamma = 1.68\text{--}2.74$), and such spectra were mostly observed in 2006 April–June when the source often exhibited both power-law and log-parabolic spectra during a single XRT

observation, even within 1 ks interval in some cases. This result may hint at extremely fast variability of the magnetic field properties in the X-ray emitting jet area of Mrk 421: a transition from the state with confinement efficiency decreasing with the particle's energy and/or higher turbulence (yielding a log-parabolic energy spectrum of electrons) into the state without these properties (power-law spectrum) and vice versa. The photon index at 1 keV sometimes showed the values $a < 1.70$, which is easier to explain in the case of some hadronic contribution to the jet matter. The photon index varied on diverse timescales, even within the 1 ks observational runs: they hardened by $\Delta a = 0.07$ in 330 s and softened by $\Delta a = 0.08$ –0.10 in 400–500 s. The hardness ratio, calculated from both log-parabolic and power-law spectra, showed a very broad range $\Delta HR = 0.92$ and unprecedentedly high percentage (26%) of values larger than $HR = 1$ (i.e., higher 2–10 keV flux compared to the soft 0.3–10 keV flux, rarely observed in HBL sources). Similar to the photon index, this parameter varied on diverse timescales and the source mostly followed a “harder-when-brighter” spectral trend during this variability. However, some small sub-samples of the spectra followed an opposite spectral trend, which is unusual for HBL sources and can be related to the emergence of soft X-ray components in the X-ray emission zone.

Along with extreme spectral variability, Mrk 421 showed a strong X-ray flaring activity, by a factor of 2–10, on timescales of few days to weeks, and a maximum-to-minimum flux ratio of 20 in the XRT band. The 0.3–10 keV count rate exceeded the threshold of 100 cts s⁻¹ (corresponding to the unabsorbed 0.3–10 keV flux of about 2.5×10^{-9} erg cm⁻² s⁻¹) for the first time since the start of *Swift* observations. We detected 118 instances of intraday 0.3–10 keV flux variability, including those with flux doubling and halving times of about 1.4 hr. On 20 occasions, flux variability was observed within 1 ks observational runs (brightenings by 4–19% in 180–900 s and declines by 6–20% in 180–960 s), generally observed in higher X-ray states and possibly related to the small-scale turbulent areas with the strongest magnetic fields in the shocked jet material.

The unabsorbed hard 0.3–2 keV flux showed a strong positive correlation with the hard 2–10 keV flux, although the latter varied more strongly, which led to interesting behavior of the source in the HR–flux plane: while it mostly showed clockwise hysteresis patterns during some flares, 2–3 cycles of the change between the opposite spectral trends were observed in some epochs (implying a change in the interplay between the particle's acceleration, synchrotron cooling, and flux variability timescales). On intraday timescales, the source generally showed a CW-type spectral evolution, as expected from earlier simulations of the stochastic acceleration of the particles behind the relativistic shock front. The X-ray and VHE fluxes often showed a correlated variability, although we found several occasions challenging one-zone SSC scenarios: a strong TeV flare was not accompanied by comparable X-ray activity and vice versa. The source sometimes underwent a UV-optical decline along with X-ray flares, possibly associated with the stochastic acceleration of electrons having a narrow initial energy distribution, shifting the distribution peak to higher energies in accord with the increasing X-ray brightness.

The period presented here shows the importance of densely sampled *Swift* and MWL observations of Mrk 421. Intensive *Swift* and *NuSTAR* campaigns in 2013 April 10–21 revealed a

giant X-ray flare in our target. Densely sampled XRT monitoring in 2006 April and June showed extreme spectral behavior, enabling us to reveal characteristic features of the physical processes responsible for the acceleration of the particles to tremendous energies and yielding the flux variability on diverse timescales. Similar intensive campaigns of nearby X-ray bright HBLs with *Swift* and other satellite/ground-based instruments in different spectral bands will be very useful for gaining a deeper understanding of blazar physics, their internal structure, and the unstable processes underlying their extreme observational features.

B.K., S.K., and L.T. acknowledge Shota Rustaveli National Science Foundation and Ilia State University for the research grant FR/377/6-290/14. P.R. acknowledges contract ASI-INAF I/004/11/0. This research has made use of the XRTDAS software, developed under the responsibility of the ASDC, Italy, and the data from the OVRO 40 m monitoring program, which is supported in part by NASA grants NNX08AW31G and NNX11A043G, and NSF grants AST-0808050 and AST-1109911. This research has made use of the VizieR catalog access tool from the CDS, Strasbourg, France. We acknowledge the use of the VHE data from long-term Whipple observations. We also acknowledge the variable star observations from the AAVSO International Database contributed by observers worldwide and used in this research. UMRAO was supported in part by a series of grants from the NSF, most recently AST 0607523, and by a series of grants from the NASA Fermi Guest Investigator program NNX 09AU16G, NNX10AP16G, NNX11AO13G, and NNX13AP18G. We thank the anonymous referee for his/her very useful comments and suggestions, which helped to improve the quality of the paper.

ORCID iDs

B. Kapanadze  <https://orcid.org/0000-0002-7146-6751>
 S. Vercellone  <https://orcid.org/0000-0003-1163-1396>
 P. Romano  <https://orcid.org/0000-0003-0258-7469>
 P. Hughes  <https://orcid.org/0000-0002-0691-3041>
 M. Aller  <https://orcid.org/0000-0003-2483-2103>
 H. Aller  <https://orcid.org/0000-0003-1945-1840>

References

- Abdo, A. A., Ackermann, M., Ajello, M., et al. 2011, *ApJ*, 736, 131
 Acciari, V. A., Aliu, E., Arlen, T., et al. 2011, *ApJ*, 738, 25
 Acciari, V. A., Aliu, E., Aune, T., et al. 2009, *ApJ*, 703, 169
 Acciari, V. A., Arlen, T., Aune, T., et al. 2014, *Aph*, 54, 1
 Ahnen, M. L., Ansoldi, S., Antonelli, L. A., et al. 2016, *A&A*, 593, 91
 Albert, J., Aliu, E., Anderhub, H., et al. 2008, *ApJ*, 674, 1037
 Aleksić, J., Alvarez, E. A., Antonelli, L. A., et al. 2012, *A&A*, 542, 100
 Aleksić, J., Ansoldi, S., Antonelli, L. A., et al. 2015a, *A&A*, 576, 126
 Aleksić, J., Ansoldi, S., Antonelli, L. A., et al. 2015b, *A&A*, 578, 22
 Aller, H. D., Aller, M. F., Latimer, G. E., et al. 1985, *ApJS*, 59, 513
 Anderhub, H., Backes, M., Biland, A., et al. 2013, *JInst*, 8, P06008
 Arnaud, K. 1996, in ASP Conf. Ser. 101, *Astronomical Data Analysis Software and Systems*, ed. G. H. Jacoby & J. Barnes (San Francisco, CA: ASP), 17
 Atwood, W. B., Abdo, A. A., Ackermann, M., et al. 2009, *ApJ*, 697, 1071
 Baloković, M., Paneque, D., Madejski, G., et al. 2016, *ApJ*, 819, 156
 Barthelmy, S. D., Barbier, L. M., Cummings, J. R., et al. 2005, *SSRv*, 120, 143
 Bessel, M. S. 1979, *PASP*, 91, 589
 Błażejowski, M., Blaylock, G., Bond, I. H., et al. 2005, *ApJ*, 630, 130
 Brinkmann, W., Sembay, S., Griffiths, R. G., et al. 2001, *A&A*, 365, L162
 Burrows, D. N., Hill, J. E., Nousek, J. A., et al. 2005, *SSRv*, 120, 165
 Cui, W. 2004, *ApJ*, 605, 662
 Falomo, R., Pian, E., & Treves, A. 2014, *A&ARv*, 22, 73

- Fossati, G., Buckley, J. H., Bond, I. H., et al. 2008, *ApJ*, 677, 906
- Fukugita, M., Shimasaku, K., & Ichikawa, T. 1995, *PASP*, 107, 945
- Furniss, A., Noda, K., Boggs, S., et al. 2015, *ApJ*, 812, 65
- Gaidos, J., Akerlof, C. W., Biller, S., et al. 1996, *Natur*, 383, 319
- Gehrels, N., Chincarini, G., Giommi, P., et al. 2004, *ApJ*, 611, 1005
- Horan, D., Acciari, V. A., Bradbury, S. M., et al. 2009, *ApJ*, 695, 596
- Kalberla, P. M. W., Burton, W. B., Hartmann, D., et al. 2005, *A&A*, 440, 775
- Kapanadze, B., Dorner, D., Romano, P., et al. 2017a, *ApJ*, 848, 103
- Kapanadze, B., Dorner, D., Romano, P., et al. 2017b, *MNRAS*, 469, 1655
- Kapanadze, B., Dorner, D., Vercellone, S., et al. 2016a, *ApJ*, 831, 102
- Kapanadze, B., Dorner, D., Vercellone, S., et al. 2016b, *MNRAS*, 461, L26
- Kapanadze, B., Dorner, D., Vercellone, S., et al. 2017c, *MNRAS*, 473, 2542
- Kapanadze, B., Romano, P., Vercellone, S., et al. 2016c, *MNRAS*, 457, 704
- Kapanadze, B., Romano, P., Vercellone, S., & Kapanadze, S. 2014, *MNRAS*, 444, 1077
- Kataoka, J., Takahashi, T., Makino, F., et al. 2000, *ApJ*, 528, 843
- Katarzyński, K., Ghisellini, G., Mastichiadis, A., Tavecchio, F., & Maraschi, L. 2006, *A&A*, 453, 47
- Krawczynski, H., Huhhes, S. B., Horan, D., et al. 2004, *ApJ*, 601, 151
- Krimm, H., Holland, S. T., Corbet, R. H. D., et al. 2013, *ApJ*, 209, 14
- Landau, R., Golisch, B., Jones, T. J., et al. 1986, *ApJ*, 308, 78
- Levine, A. M., Bradt, H., Cui, W., et al. 1996, *ApJL*, 469, L33
- Macomb, N., Akerlof, C. W., Aller, H. D., et al. 1995, *ApJL*, 449, L99
- Mannheim, K. 1993, *A&A*, 269, 60
- Marscher, A. P., & Gear, W. K. 1985, *ApJ*, 298, 114
- Massaro, E., Perri, M., Giommi, P., & Nesci, R. 2004, *A&A*, 413, 489
- Massaro, F., Paggi, A., & Cavaliere, A. 2011, *ApJL*, 742, L32
- Massaro, F., Tramacere, A., Cavaliere, A., Perri, M., & Giommi, P. 2008, *A&A*, 448, 861
- Mastichiadis, A., & Moraitis, K. 2008, *A&A*, 491, L37
- Matsuoka, M., Kawasaki, K., Ueno, S., et al. 2009, *PASJ*, 61, 999
- Max-Moerbeck, W., Richards, J. L., Hovatta, T., et al. 2014, *MNRAS*, 445, 437
- Mizuno, Y., Pohl, M., Hiemiec, J., et al. 2014, *MNRAS*, 439, 3490
- Mücke, A., Protheroe, R. J., Engel, R., Rachen, J. P., & Stanev, T. 2003, *APH*, 18, 593
- Nilsson, K., Pasanen, M., Takalo, L. O., et al. 2007, *A&A*, 475, 199
- Padovani, P., & Giommi, P. 1995, *ApJ*, 444, 567
- Page, M., Kuin, N. P. M., Breeveld, A. A., et al. 2013, *MNRAS*, 436, 1684
- Pian, E., Fruchter, A. S., Bergeron, L. E., et al. 1998, *ApJL*, 492, L17
- Prezioso, S. 2013, PhD thesis, Univ. Pisa, <http://etd.adm.unipi.it/t/etd-10092013-064224/>
- Punch, M., Akerlof, C. W., Cawley, M. F., et al. 1992, *Natur*, 358, 477
- Ravasio, M., Tagliaferri, G., Ghisellini, G., & Tavecchio, F. 2004, *A&A*, 424, 841
- Rebillot, P. F., Badran, H. M., Blaylock, G., et al. 2006, *ApJ*, 641, 740
- Richards, J. L., Max-Moerbeck, W., Pavlidou, V., et al. 2011, *ApJS*, 194, 29
- Romano, P., Campana, S., Chincarini, G., et al. 2006, *A&A*, 456, 917
- Romero, G. E., Cellone, S. A., & Combi, J. A. 1999, *A&AS*, 135, 477
- Roming, P. W. A., Kennedy, T. E., Mason, K. O., et al. 2005, *SSRv*, 120, 95
- Saito, S., Stawarz L., Tanaka, Y. T., et al. 2013, *ApJL*, 766, L11
- Shukla, A., Chitnis, V. R., Singh, B. B., et al. 2015, *ApJ*, 798, 2
- Sinha, A., Shukla, A., Saha, L., et al. 2016, *A&A*, 591, 83
- Smith, P. S., Montiel, E., Rightley, S., et al. 2009, arXiv:0912.3621
- Sokolov, A., Marscher, A. P., & McHardy, I. M. 2004, *ApJ*, 613, 725
- Steinke, B. 2012, PhD thesis, Tech. Univ. Munich, <https://mediatum.ub.tum.de/doc/1097511/document.pdf>
- Takahashi, T., Kataoka, J., Madejski, G., et al. 1996, *ApJL*, 470, L89
- Tammy, D., & Duffy, P. 1992, *MNRAS*, 393, 1063
- Tanihata, C., Kataoka, J., Takahashi, T., & Madejski, G. M. 2004, *ApJ*, 601, 759
- Tavecchio, F., Maraschi, L., Pian, E., et al. 2001, *ApJ*, 554, 725
- Tramacere, A., Giommi, P., Perri, M., Verrecchia, F., & Tosti, G. 2009, *A&A*, 501, 879
- Tramacere, A., Massaro, E., & Taylor, A. 2011, *ApJ*, 739, 66
- Urry, C. M., & Padovani, P. 1995, *PASP*, 107, 803
- Vaughan, S., Edelson, R., Warwick, R. S., & Uttley, P. 2003, *MNRAS*, 345, 1271
- Virtanen, J. J. P., & Vainio, R. 2005, *ApJ*, 621, 313